

# Regulation of electron delocalization between flower-like (Co, Ni)-MOF array and WO<sub>3</sub>/W photoanode for effective photoelectrochemical water splitting

Pengyu Dong <sup>a,\*</sup>, Jinkang Pan <sup>a</sup>, Lihua Zhang <sup>a</sup>, Xiu-Li Yang <sup>a</sup>, Ming-Hua Xie <sup>a,\*</sup>, Jinlong Zhang <sup>b,\*</sup>

<sup>a</sup> Key Laboratory for Advanced Technology in Environmental Protection of Jiangsu Province, Yancheng Institute of Technology, Yancheng 224051, China

<sup>b</sup> Key Laboratory for Advanced Materials and Institute of Fine Chemicals, School of Chemistry & Molecular Engineering, Shanghai Engineering Research Center for Multi-media Environmental Catalysis and Resource Utilization, East China University of Science and Technology, 130 Meilong Road, Shanghai 200237, China

## ARTICLE INFO

### Keywords:

PEC water splitting  
Photoanode  
Electron delocalization  
(Co  
Ni)-MOF  
WO<sub>3</sub>/W thin film

## ABSTRACT

A stable heterometallic (Co, Ni)-MOF array with a 3D hierarchical flower-like morphology was coated onto the coral-like WO<sub>3</sub>/W thin film. The optimal (Co, Ni)-MOF/WO<sub>3</sub>/W photoanode exhibits a high photocurrent density of 2.96 mA cm<sup>-2</sup> at 1.23 V in the 0.5 M Na<sub>2</sub>SO<sub>4</sub> solution and the photoelectrochemical (PEC) cell displays an excellent solar-to-hydrogen (STH) efficiency (2.17 %) under AM 1.5 G solar light. Moreover, the separation behavior and spatial distribution of photogenerated charges have been demonstrated by photo-assisted Kelvin probe force microscopy (KPFM). Furthermore, the shift of the d-band center and the change of Gibbs free energy for oxygen evolution reaction (OER) are realized by density functional theory (DFT) calculations. Overall, the coupling effect of these ions of Co<sup>2+</sup>, O<sup>2-</sup>, Ni<sup>2+</sup>, and W<sup>6+</sup> could result in an electron delocalization in the (Co, Ni)-MOF/WO<sub>3</sub>/W photoanode, boosting the OER activity and finally improving the PEC water splitting performance.

## 1. Introduction

Among the most promising methods for producing hydrogen (H<sub>2</sub>) from solar power, the photoelectrochemical (PEC) water-splitting processes have earned a great deal of consideration. The PEC technology depends on an integrated photoelectrode, whereupon light absorption and water electrolysis occur simultaneously on the same module, thus providing the promise of solar energy conversion [1,2].

The photoanodes of PEC systems have been constructed using a variety of semiconductors during recent decades. Until now, some metal oxide semiconductor materials have been thought to be viable options for photoanodes, such as TiO<sub>2</sub>, ZnO, Fe<sub>2</sub>O<sub>3</sub>, BiVO<sub>4</sub>, and WO<sub>3</sub> [3]. Among these candidates, both TiO<sub>2</sub> and ZnO are UV-light-driven photoanodes due to their wide band gaps, which greatly limits the light-harvesting ability of solar energy, resulting in low efficiency [4]. In particular, the serious photo-corrosion phenomenon limits the longevity of ZnO-based photoelectrodes [5]. Besides, Fe<sub>2</sub>O<sub>3</sub> has serious limitations in terms of short hole diffusion length (2–4 nm), resulting in a high electron–hole recombination rate and poor PEC performance [6]. BiVO<sub>4</sub> photoelectrode with a band gap of ~2.4 eV has high theoretical

photocurrent density (7.5 mA cm<sup>-2</sup>) and solar-to-hydrogen (STH) efficiency (9.2 %) under AM 1.5 G solar light illumination (100 mW cm<sup>-2</sup>) [7,8]. However, the primary obstacles preventing BiVO<sub>4</sub> from practical application are its low electrical conductivity and slow surface reaction kinetics for water oxidation, resulting in the actual PEC property being far less than anticipated [9]. WO<sub>3</sub> is a visible-light-driven n-type semiconductor with a band gap of 2.5–2.8 eV that has the potential to use 12 % of solar radiation [10]. WO<sub>3</sub> has garnered a lot of interest because it has the following advantages, such as a long hole diffusion length (ca. 150 nm) compared with that of Fe<sub>2</sub>O<sub>3</sub> (2–4 nm) and TiO<sub>2</sub> (~100 nm), strong chemical stability in aqueous solutions, particularly in acid solutions, excellent electron mobility (~12 cm<sup>2</sup> V<sup>-1</sup> s<sup>-1</sup>), heavy oxidative capacity, and straightforward preparation techniques [11–13]. Moreover, the maximal STH efficiency of WO<sub>3</sub> photoanode is 4.8 %, theoretically significantly greater than that of TiO<sub>2</sub> (2.2 %) [4]. Nevertheless, the PEC efficiency of WO<sub>3</sub> photoanode is still considerably insufficient for practical implementation, which is primarily owing to the severe charge recombination and poor charge transfer, linked to the surface recombination rate constant ( $k_{\text{rec}}$ ) and the carrier transfer rate constant ( $k_{\text{tr}}$ ) [14]. The charge transfer efficiency  $\eta_{\text{trans}} = k_{\text{tr}}/(k_{\text{tr}} + k_{\text{rec}})$  of the

\* Corresponding authors.

E-mail addresses: [dongpy11@gmail.com](mailto:dongpy11@gmail.com) (P. Dong), [minghxie@163.com](mailto:minghxie@163.com) (M.-H. Xie), [jlzhang@ecust.edu.cn](mailto:jlzhang@ecust.edu.cn) (J. Zhang).



carrier flow into the surface that is utilized in the oxygen evolution reaction (OER) or hydrogen evolution reaction (HER) is determined by the competitive relationship between  $k_{\text{rec}}$  and  $k_{\text{tr}}$  [15]. Consequently, the rational structural design and morphology control of  $\text{WO}_3$  photoanodes are beneficial to solving this issue and boosting the PEC water splitting performance, including improvement of light absorption ability through electron-donating elemental doping or introducing oxygen vacancies, promotion of the consumption of photoinduced holes by exposing them to high-energy crystal surfaces, and enhancement of the electrical conductivity and charge separation efficiency through various strategies [16–18]. In particular, implementing OER co-catalysts onto the  $\text{WO}_3$  surface has significantly increased the charge separation and transfer efficiency while also improving the water oxidation kinetics [19]. Moreover, co-catalysts can be introduced to decrease the overpotential that inhibits peroxospecies formation, which might be due to the rapid transfer of photoinduced holes to  $\text{H}_2\text{O}$  or  $\text{OH}^-$  at a lower water oxidation overpotential, facilitating the oxygen-evolution reaction and thus suppressing the formation of peroxospecies [20]. Besides that, nanostructured  $\text{WO}_3$  photoanode (e.g., nanoplate arrays) could benefit the charge separation by decreasing the nanoparticle size, thereby promoting the photoinduced holes to migrate to the  $\text{WO}_3$ /electrolyte interface [21]. Additionally, the separation and transfer of photoinduced charges of  $\text{WO}_3$  photoanode could be accelerated by coupling narrow band-gap semiconductors, such as  $\text{Cu}_2\text{O}$  [22],  $\text{CoO}_x$  [23], conducting polymers (CPs) [24],  $\text{Sb}_2\text{S}_3$  [25], and  $\text{BiVO}_4$  [19,26,27]. On the other hand, the slow charge carrier transfer efficiency ( $\eta_{\text{trans}}$ ) at the electrolyte/semiconductor interface and insufficient surface catalytic active sites pose a challenge for the  $\text{WO}_3$  photoanode [10,18].

In terms of periodic network structures, metal-organic frameworks (MOFs) are considered crystalline porous materials. Compared with the common water splitting co-catalysts (e.g.,  $\text{CoOOH}$ ,  $\text{NiOOH}$ ), visible light receptive MOFs as co-catalysts for semiconductor photoanodes could exhibit the following advantages, such as (i) visible light receptive MOF has the potential to enhance optical harvesting efficiency, (ii) the MOF's porous structure wouldn't obstruct the sensitive semiconductor's optical absorption channel, (iii) accelerated charge transfer may be achieved by easily transporting photo-excited electrons from the MOF structure to a sensitized semiconductor through a well-connected MOF/semiconductor interface, which is dependent on many factors such as the contact interface between them and the thickness of the thin films, and (iv) the MOF's porous structure with the large surface area could allow the ions, electrolyte solution, and the produced gas bubble diffusion to guarantee the structural robustness for stable and superior PEC performance [28–30]. As is well known, negatively charged coordinated groups or nonmetal atoms can modify the coordination environment of the metal center of MOFs, which in turn can optimize the binding energies of intermediates through the suitable *d*-band center [31]. Because of their flexible organic ligands and tunable organometallic ions or clusters, regular structured MOFs in the newly developed photo-electrode demonstrate exceptional synthesis adjustability. This helps to satisfy the requirements for both PEC performance enhancement and the modification of conventional photo-electronic materials [32]. It has been demonstrated that decorating semiconductor photoanode surfaces with OER catalysts is a useful method for lowering the reaction overpotential and accelerating surface OER kinetics, which enhances PEC performance for water splitting [33]. (Co, Ni)-based bimetallic MOFs are used as the OER catalysts, which could effectively extract photo-generated holes from semiconductor photoanodes to their active sites, hence preventing charge recombination by quickly consuming the surface holes during the water oxidation process [34]. In addition, it is feasible to design a simple strategy to synthesize bimetallic (Co, Ni)-MOF because H atoms in ligands of MOF could be readily replaceable by Co and Ni ions.

Considering the above characteristics of  $\text{WO}_3$  photoanode and (Co, Ni)-MOF, it is desired to construct (Co, Ni)-MOF-modified  $\text{WO}_3$  photoanode to boost its PEC performance. In this work, a coral-like

nanostructured  $\text{WO}_3/\text{W}$  thin film with tight contact and strong binding force between  $\text{WO}_3$  and metal W foil as substrate was prepared through an electrochemical anodization method followed by a calcination process, and subsequently a (Co, Ni)-MOF/ $\text{WO}_3/\text{W}$  photoanode was constructed and achieved by solvothermal deposition of (Co, Ni)-MOF with a flower-like nanoplate array morphology onto the  $\text{WO}_3/\text{W}$  thin film. Highly improved photoanode performance can be achieved by regulating the electron delocalization in the (Co, Ni)-MOF/ $\text{WO}_3/\text{W}$  photoanode for effective STH conversion.

## 2. Experimental

### 2.1. Preparation of (Co, Ni)-MOF/ $\text{WO}_3/\text{W}$ photoanode

First of all, the substrate of  $\text{WO}_3/\text{W}$  thin film was synthesized by an anodic oxidation process, which was produced in a previous publication with minor adjustments [35], and the detailed preparation procedure was presented in the [Supplementary material](#). Secondly, a homogenized dispersion was created in the 50 mL Teflon container by gradually adding and stirring different chemicals, including 0.25 mmol  $\text{CoCl}_2 \cdot 6 \text{ H}_2\text{O}$  (99.0 %), 0.125 mmol  $\text{Ni}(\text{NO}_3)_2 \cdot 6 \text{ H}_2\text{O}$  (99.0 %), 0.375 mmol terephthalic acid (99.0 %), 9 mL *N*, *N*'-dimethylformamide (DMF), 0.5 mL ethanol, and 0.5 mL deionized water. The Teflon-lined autoclave was then heated to 140 °C and maintained there for 48 h. Once the temperature had dropped to room temperature, the resulting thin films were then allowed to naturally dry after being submerged in ethanol and deionized water, respectively. At last, the (Co<sub>1</sub>, Ni<sub>0.5</sub>)-MOF modified  $\text{WO}_3/\text{W}$  photoanode was realized and assigned the designation (Co, Ni)-MOF/ $\text{WO}_3/\text{W}$ . Comparatively, the equivalent  $\text{CoCl}_2 \cdot 6 \text{ H}_2\text{O}$  and  $\text{Ni}(\text{NO}_3)_2 \cdot 6 \text{ H}_2\text{O}$  were added to generate the single-metal Co-MOF/- $\text{WO}_3/\text{W}$  and Ni-MOF/ $\text{WO}_3/\text{W}$  photoanode thin films, respectively, and other steps were the same as for the fabrication of (Co, Ni)-MOF/ $\text{WO}_3/\text{W}$  photoanode. Additionally, different atomic ratios of Co to Ni and thicknesses of (Co, Ni)-MOF/ $\text{WO}_3/\text{W}$  photoanode thin films were produced, and the dosage details are listed in [Table S1](#). The corresponding photographs of the photoanode thin films in their prepared state are displayed in [Fig. S1](#). To compare the PEC performance of the  $\text{WO}_3/\text{W}$  substrate and the traditional  $\text{WO}_3$  substrate,  $\text{WO}_3$  films on commercial fluorine-doped tin oxide (FTO) coated glasses were prepared by a hydrothermal method, which was labeled as  $\text{WO}_3/\text{FTO}$ . In addition, (Co, Ni)-MOF/ $\text{WO}_3/\text{FTO}$  films were prepared by a hydrothermal method for comparison. The preparation details are described in the [Supplementary material](#).

### 2.2. Materials characterization

Using Cu K $\alpha$  irradiation ( $\lambda = 1.5418 \text{ \AA}$ ), X-ray diffraction (XRD) was used to identify the crystal structures of the produced samples (PANalytical X'Pert<sup>3</sup> Powder). NICOLET NEXUS-670 was used to record Fourier transforms infrared (FTIR) spectra. Using a 532 nm laser as the light source, Raman spectra were acquired on a Thermo Fischer DXR. BaSO<sub>4</sub> was used as a reference for recording UV-Vis diffuse reflectance spectroscopy (DRS) (Shimadzu, UV-3600). Using an Al K $\alpha$  ( $h\nu = 1486.6 \text{ eV}$ ) and a hemispherical electron energy analyzer, an X-ray source was used to assess X-ray photoelectron spectroscopy (XPS) analysis (Thermo Scientific, ESCALAB 250Xi). Using an energy-dispersive spectroscopy (EDS)-equipped FEI Nova NanoSEM 450 scanning electron microscope (SEM) (X-MaxN 80T IE250), the morphology was examined. A Brucker Dimension Icon microscope was used to measure atomic force microscopy (AFM). Materials Studio provided the anticipated Bravais–Friedel–Donnay–Harker (BFDH) crystal shape. The Micromeritics ASAP 2020 analyzer was used to assess the N<sub>2</sub> adsorption-desorption isotherms at 77 K. A Thera Flex contact angle analyzer was used to measure the water's contact angle with the product. Kelvin Probe Force Microscopy (KPFM) measurements were conducted on the Bruker MM8 system, and a halogen lamp (Bruker-NMB) was employed

as the light source. Thermo Scientific K-Alpha instrument was used for high-resolution valence band XPS (VB-XPS) measurements. The corresponding measurement details were described in the Supplementary material.

### 2.3. PEC measurements

On the electrochemical workstation (CHI660E), a three-electrode setup with a quartz cell was used to perform PEC measurements. The as-obtained thin films, which had a  $2.2 \text{ cm}^2$  available surface area, were employed as photoanodes. A Pt sheet was utilized as the cathode, and an Ag/AgCl (saturated KCl) reference electrode was employed. For PEC measurement, a simulated sunshine Xe lamp (CEL-HXF300) with an AM 1.5 G filter was used as the lamp housing (Fig. S2). The optical power meter (Newport, Model 843-R) confirmed that the light power density, or light intensity, had been adjusted to be  $100 \text{ mW cm}^{-2}$ . The CHI660E electrochemical workstation was used to perform the transient photocurrent responses, Mott-Schottky plots, electrochemical impedance spectroscopy (EIS), and linear sweep voltammetry (LSV) curves at a scan rate of  $10 \text{ mV s}^{-1}$ . Using an Omno151 monochromator to produce single-wavelength light, the incident photon-to-current efficiency (IPCE) was evaluated in the same electrochemical workstation with an applied potential of  $0.62 \text{ V}$  vs. Ag/AgCl. Thus, the IPCE could be expressed in the following Eq. (1) [18].

$$\text{IPCE (\%)} = \frac{J(\text{mA cm}^{-2}) \times 1240(\text{V nm})}{\lambda(\text{nm}) \times J_{\text{light}}(\text{mW cm}^{-2})} \times 100\% \quad (1)$$

where  $J$  represents the photocurrent density ( $\text{mA cm}^{-2}$ ),  $\lambda$  represents the wavelength (nm) of the incident light, and  $J_{\text{light}}$  refers to the intensity of light at a certain wavelength ( $\text{mW cm}^{-2}$ ) measured from the Newport 843-R optical power meter.

The following Nernst equation describes the transformation of potential vs. Ag/AgCl into values vs. reversible hydrogen electrode (RHE).

$$E_{\text{RHE}} = E_{\text{Ag/AgCl}} + 0.059pH + 0.197 \quad (2)$$

where  $E_{\text{RHE}}$  represents the potential vs. RHE,  $E_{\text{Ag/AgCl}}$  represents the experimentally measured potential vs. Ag/AgCl, and  $0.197 \text{ V}$  is the standard potential vs. Ag/AgCl measured at room temperature ( $25^\circ \text{C}$ ).

The following equation was used to determine the applied bias photon-to-current efficiency (ABPE) assuming 100 % Faradaic efficiency [36].

$$\text{ABPE (\%)} = \frac{J \times (1.23 - V_{\text{bias}})}{P_{\text{sun}}} \times 100\% \quad (3)$$

where  $J$  denotes the photocurrent density ( $\text{mA cm}^{-2}$ ),  $V_{\text{bias}}$  represents the applied voltage (V, vs. RHE), and  $P_{\text{sun}}$  is the energy flux of the simulated sunlight ( $100 \text{ mW cm}^{-2}$ ).

### 2.4. PEC water splitting

A 120 mL quartz reactor chamber filled with  $0.5 \text{ M Na}_2\text{SO}_4$  solution was used to assess the PEC water splitting activity. The CHI660E electrochemical workstation was employed to carry out the PEC water-splitting measurement with an externally applied bias voltage ( $0.62 \text{ V}$  vs. Ag/AgCl). The light source was an AM 1.5 G filter-equipped Xe lamp (CEL-HXF300,  $100 \text{ mW cm}^{-2}$ ) that mimicked sunshine. Prior to the PEC reaction, dissolved oxygen ( $\text{O}_2$ ) was eliminated from the system by purging the solution with a high-purity Ar gas flow. For the PEC process, a  $0.5 \text{ mL}$  gas sample was taken every hour to measure the amount of  $\text{H}_2$  and  $\text{O}_2$ . Using Ar as a carrier gas,  $\text{O}_2$  and  $\text{H}_2$  were examined at  $60^\circ \text{C}$  in gas chromatography (GC-2011, 5 Å molecular sieve column).

The Faradaic efficiency (FE) is determined according to the following Eq. (4):

$$\text{FE} = \frac{\alpha nF}{I \times t} \times 100\% \quad (4)$$

where  $\alpha$  is the number of electrons transferred accompanied by a molecule product.  $n$  presents the actual mole number of the product, and  $F$  presents the Faradaic constant ( $96485.33 \text{ C mol}^{-1}$ ).  $I$  is the recorded photocurrent and  $t$  is the test time.

The STH efficiency was calculated based on the evolution rate of hydrogen ( $r_{\text{H}_2}$ ,  $\mu\text{mol s}^{-1}$ ), which could be expressed as Eq. (5) [36].

$$\text{STH (\%)} = \frac{\text{Output energy as H}_2}{\text{Incident solar energy}} = \frac{r_{\text{H}_2} \times \Delta G}{P_{\text{sun}} \times S} \times 100\% \quad (5)$$

where  $S$  is the irradiated area of the PEC reactor, which is  $3.14 \text{ cm}^2$  in this work; Gibbs energy ( $\Delta G$ ) is  $237 \text{ kJ mol}^{-1}$ .

### 2.5. DFT calculations

Vienna *ab initio* simulation software (VASP) was used to perform density functional theory (DFT) computations based on the plane-wave basis sets using the projector augmented-wave technique [37]. Using the Perdew-Burke-Ernzerhof (PBE) parametrization, a generalized gradient approximation (GGA) was employed to solve the exchange-correlation potential. Grimme's DFT-D3 model was also adopted, along with the van der Waals correction. Following previous works [38,39], the Co and Ni element is given an effective Hubbard Ueff of  $3.32$  and  $6.4 \text{ eV}$ , respectively. Since there are two possible adsorption sites on the interface, we assessed the adsorption of  $\text{O}^*$ ,  $\text{OH}^*$ , and  $\text{OOH}^*$  on the Co and Ni sites, respectively. The  $520 \text{ eV}$  energy threshold was chosen. A  $2 \times 1 \times 1$  Monkhorst-Pack mesh centered on the  $\Gamma$ -axis was used to sample the Brillouin-zone integration. The structures were completely relaxed when the energy convergent standard reached  $10^{-5} \text{ eV}$  and the maximum force applied to each atom was less than  $0.01 \text{ eV}/\text{\AA}$ . The system's periodic pictures were spaced out by around  $20 \text{ \AA}$ , and this area was referred to as the vacuum layer region. The quantum mechanical harmonic approximation was employed to calculate the adjustments for the free energy of the adsorbed species while accounting for the vibrational frequencies. Free energy diagrams are created by modifying the total energy of  $\text{O}_2$  in the gas phase following the previously discussed formation of Gibbs free energy of  $\text{H}_2\text{O}$  in a liquid state [40]. Then, Christensen's correction method is used to adjust the systems with adsorbates' total energies.

The temperature factor ( $D_{\text{H}}$ ), zero-point energy ( $E_{\text{ZPE}}$ ), and entropy effect (TS) were added to the total ground state energy ( $E_{\text{total}}$ ) determined using DFT calculations to estimate the free energy (G) of each adsorption intermediate. This was done using the formula  $G = E_{\text{total}} + E_{\text{ZPE}} + D_{\text{H}} - TS$ , in which TS is the contribution of entropy to the free energy at  $298 \text{ K}$ . The entropies and  $E_{\text{ZPE}}$  of the OER species adsorbed on the interface were then calculated.

## 3. Results and discussion

### 3.1. Structural characterization and morphological features

According to Fig. 1a, XRD patterns collected from the thin films of  $\text{WO}_3/\text{W}$ , Co-MOF/ $\text{WO}_3/\text{W}$ , Ni-MOF/ $\text{WO}_3/\text{W}$ , and (Co, Ni)-MOF/ $\text{WO}_3/\text{W}$  were utilized to identify the crystal phases. Based on the XRD results, the  $\text{WO}_3/\text{W}$  thin film exhibits a monoclinic structure of  $\text{WO}_3$  (PDF#43-1035) in addition to the metal W phase (PDF#89-2767) [41]. Additionally, the XRD pattern of (Co, Ni)-MOF was simulated based on its Crystallographic Information File (CIF). It expectedly shows the characteristic diffraction peaks located at  $8.8^\circ$ ,  $14.2^\circ$ ,  $15.8^\circ$ , and  $17.8^\circ$  in Fig. S3, which can be indexed to the (200), (001), (-201), and (400) crystallographic planes of (Co, Ni)-MOF linked via terephthalate ligands, respectively. In addition, the XRD patterns of power samples of Co-MOF, Ni-MOF, ( $\text{Co}_1, \text{Ni}_1$ )-MOF, and ( $\text{Co}_1, \text{Ni}_{0.5}$ )-MOF are illustrated in Fig. S3, in which the diffraction peaks matched well with the simulated (Co, Ni) bimetal MOF are obviously observed, further confirming the successful preparation of (Co, Ni)-MOF. To investigate the feature bands in the as-prepared thin films, FTIR spectra were performed (Fig. 1b). The

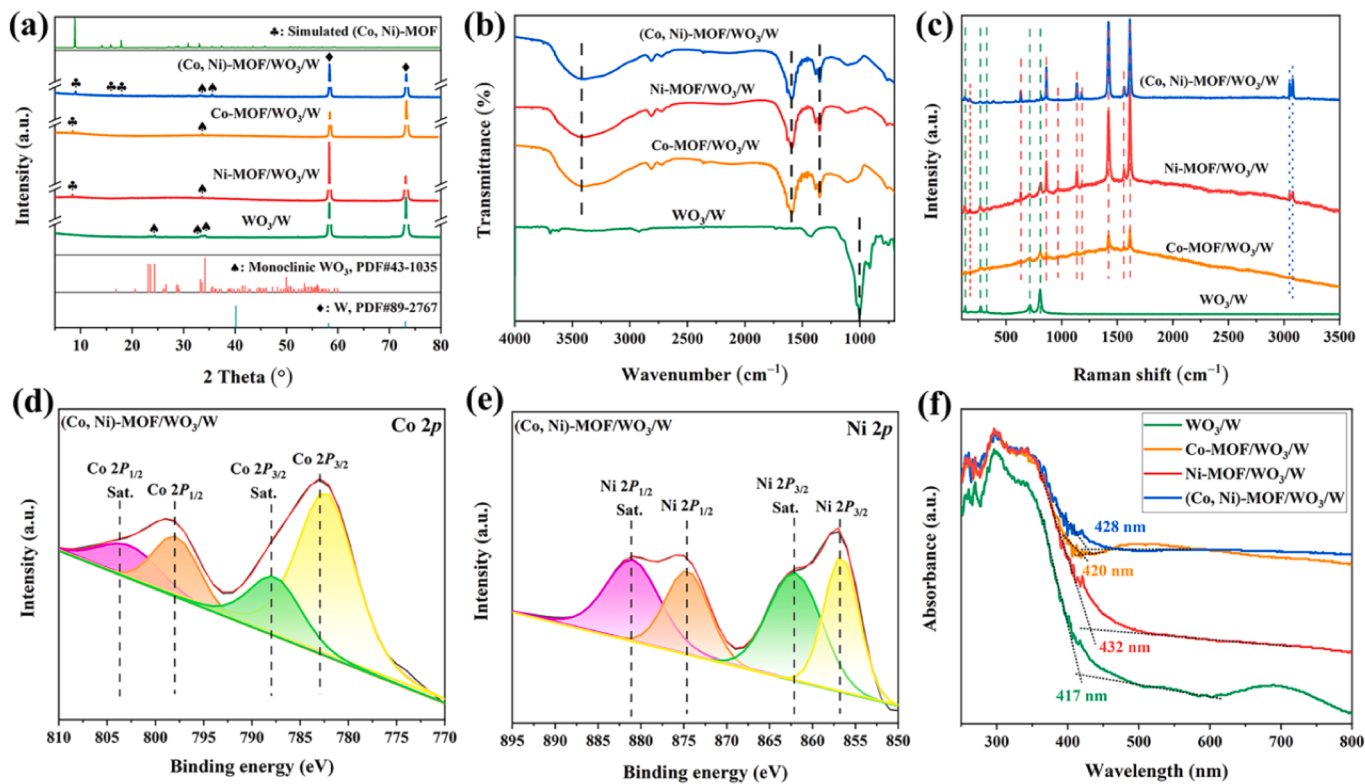


**Fig. 1.** (a) XRD patterns, (b) FTIR spectra, (c) Raman spectra of the  $\text{WO}_3/\text{W}$ ,  $\text{Co}-\text{MOF}/\text{WO}_3/\text{W}$ ,  $\text{Ni}-\text{MOF}/\text{WO}_3/\text{W}$ , and  $(\text{Co}, \text{Ni})-\text{MOF}/\text{WO}_3/\text{W}$  thin films. (d) High-resolution Co 2p, and (e) Ni 2p XPS spectra of the  $(\text{Co}, \text{Ni})-\text{MOF}/\text{WO}_3/\text{W}$  thin film. (f) UV–Vis DRS spectra of these thin-film samples.

intensive peak at  $1002\text{ cm}^{-1}$  could be assigned to the stretching mode of the W–O groups in the  $\text{WO}_3/\text{W}$  thin films [42]. There are asymmetrical stretching vibrations ( $1594\text{ cm}^{-1}$ ) and symmetrical stretching vibrations ( $1352\text{ cm}^{-1}$ ) of  $-\text{COO}^-$  in terephthalate anions [43], demonstrating the coordination of the  $-\text{COO}^-$  of terephthalate anions with  $\text{Co}^{2+}/\text{Ni}^{2+}$  in a bidentate configuration [44,45]. The Raman spectra of all the as-prepared photoanode thin films are displayed in Fig. 1c. In all samples, the region of  $1100\text{--}1700\text{ cm}^{-1}$  reveals five bands at  $1134$ ,  $1178$ ,  $1422$ ,  $1559$ , and  $1615\text{ cm}^{-1}$ . These modes may be attributed to the aromatic ring in-plane vibrations, in which the two on the lower frequency are associated with the ring deformation modes, and the three on the higher frequency are ascribed to the stretching modes [46]. The peaks at  $865$  and  $630\text{ cm}^{-1}$  may be associated with the out-of-plane deformation of the C–H groups in the terephthalate ligands [47]. However, the peaks at around  $270$ ,  $326$ ,  $706$ , and  $809\text{ cm}^{-1}$  can be ascribed to the monoclinic  $\text{WO}_3$  [48]. The peaks at  $134$ ,  $175$ , and  $964\text{ cm}^{-1}$  can be attributed to the lattice mode of  $\text{WO}_3$ , the M–O bonds ( $M = \text{Co}$  or  $\text{Ni}$ ), and the O–H bending vibration, respectively [49]. The peaks at around  $3050$  and  $3075\text{ cm}^{-1}$  can be ascribed to the –CH stretching modes [50]. It further confirms that the obtained bimetallic  $(\text{Co}, \text{Ni})-\text{MOF}/\text{WO}_3/\text{W}$  photoanode thin films possess almost the same Raman bands with the single-metal  $\text{Co}-\text{MOF}/\text{WO}_3/\text{W}$  as well as  $\text{Ni}-\text{MOF}/\text{WO}_3/\text{W}$ , which is in agreement with the XRD results. XPS analysis was conducted on  $(\text{Co}, \text{Ni})-\text{MOF}/\text{WO}_3/\text{W}$  and  $\text{WO}_3/\text{W}$  thin films to determine their chemical bonding states. As illustrated in Fig. S4a, Co, Ni, C, O, and W elements are observed in the full spectrum for the  $(\text{Co}, \text{Ni})-\text{MOF}/\text{WO}_3/\text{W}$  thin film. In comparison with the  $\text{WO}_3/\text{W}$  thin film, the W 4  $f_{7/2}$  and W 4  $f_{5/2}$  peaks for  $(\text{Co}, \text{Ni})-\text{MOF}/\text{WO}_3/\text{W}$  shifted to higher binding energy by ca.  $0.3\text{ eV}$  (Fig. S4d) because of the tough interaction formed between the  $(\text{Co}, \text{Ni})-\text{MOF}$  and  $\text{WO}_3/\text{W}$  thin films during the solvothermal process. In addition, the peak appears at about  $797.9$  and  $782.9\text{ eV}$  (Fig. 1d) could be assigned to  $\text{Co } 2p_{1/2}$  and  $\text{Co } 2p_{3/2}$ , respectively, whereas the other double peaks at  $787.9$  and  $803.7\text{ eV}$  are associated with shake-up satellites (sat.), which are the feature peaks of

the oxidation state of Co (II) [51]. As can be seen from the high-resolution Ni 2p XPS spectrum in Fig. 1e, the fitting peaks at  $873.7$  and  $855.8\text{ eV}$  correspond to  $\text{Ni } 2p_{1/2}$  and  $\text{Ni } 2p_{3/2}$ , respectively. Furthermore, the double fitting peaks at  $880.1$  and  $861.7\text{ eV}$  could be ascribed to the shake-up satellites (sat.) of  $\text{Ni } 2p_{1/2}$  and  $\text{Ni } 2p_{3/2}$ , respectively, suggesting the feature peaks of the oxidation state of Ni (II) [52]. Consequently, these results demonstrate that Co and Ni ions are mainly presented in the valence states of  $\text{Co}^{2+}$  and  $\text{Ni}^{2+}$  in the as-prepared  $(\text{Co}, \text{Ni})-\text{MOF}/\text{WO}_3/\text{W}$  photoanodes thin films. The optical absorbance properties of as-prepared photoanodes were determined by UV–Vis DRS. From Fig. 1f, it is observed that the  $\text{WO}_3/\text{W}$  thin film shows an absorbance edge around  $417\text{ nm}$ , which identifies the energy band gap ( $2.97\text{ eV}$ ) of the  $\text{WO}_3$  semiconductor. Besides that, broadband is observed from  $600$  to  $800\text{ nm}$  in the  $\text{WO}_3/\text{W}$  thin film, which might be associated with the visible light absorption of the metal W sheet. Compared with the  $\text{WO}_3/\text{W}$  thin film, the absorption edges of  $\text{Co}-\text{MOF}/\text{WO}_3/\text{W}$ ,  $\text{Ni}-\text{MOF}/\text{WO}_3/\text{W}$ , and  $(\text{Co}, \text{Ni})-\text{MOF}/\text{WO}_3/\text{W}$  thin films are red-shifted to  $432$ ,  $420$ , and  $428\text{ nm}$ , respectively. The redshift of the absorption edge might be attributed to the strong electronic coupling between MOFs and  $\text{WO}_3/\text{W}$  thin film. Moreover, it is observed that the visible-light absorption intensity of  $\text{Ni}-\text{MOF}/\text{WO}_3/\text{W}$  and  $(\text{Co}, \text{Ni})-\text{MOF}/\text{WO}_3/\text{W}$  is much higher than that of  $\text{Co}-\text{MOF}/\text{WO}_3/\text{W}$  and  $\text{WO}_3/\text{W}$  thin films in the range of  $400\text{--}800\text{ nm}$ , indicating that much more visible light could be absorbed due to the introduction of Ni-MOF and  $(\text{Co}, \text{Ni})-\text{MOF}$ .

SEM was employed to examine the surface morphology feature of the as-prepared thin films. As displayed in Fig. 2a and Fig. S5a, a coral-like nanostructure is presented in the  $\text{WO}_3/\text{W}$  thin film. Fig. 2b and Fig. S5b indicate that  $\text{Co}-\text{MOF}$  displays a compact mushroom-like morphology that is made up of nanoplates, which might prevent the light absorption ability from reaching the covered  $\text{WO}_3/\text{W}$  thin film. From Fig. 2c and Fig. S5c, the  $\text{Ni}-\text{MOF}$  shows a spherical flower-shaped morphology composed of ultrathin nanosheets. Fig. 2d and Fig. S5d illustrate that the  $(\text{Co}, \text{Ni})-\text{MOF}$  array had a 3D hierarchical flower-like morphology

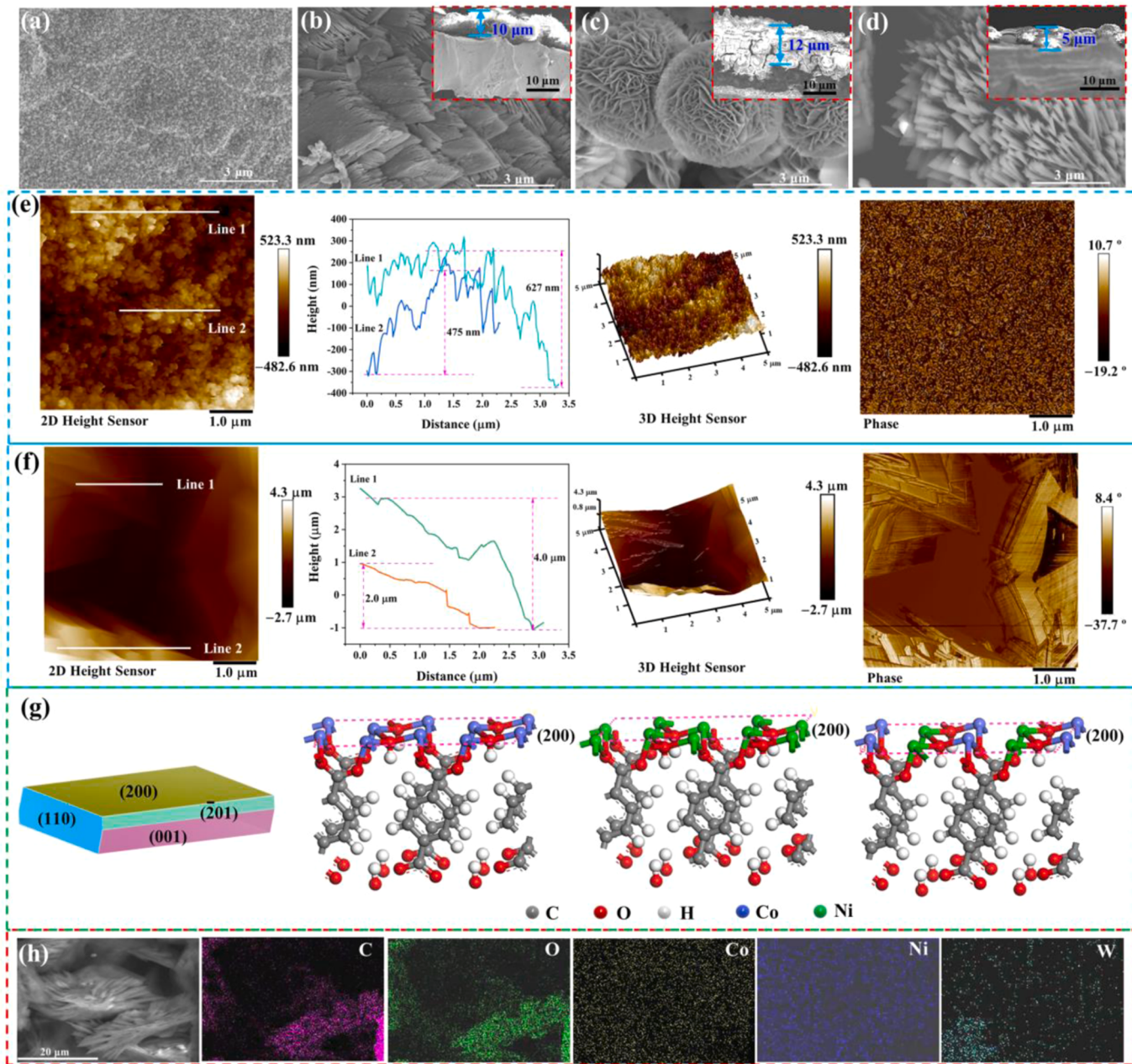


**Fig. 2.** SEM images of (a)  $\text{WO}_3/\text{W}$ , (b) Co-MOF/ $\text{WO}_3/\text{W}$ , (c) Ni-MOF/ $\text{WO}_3/\text{W}$ , and (d) (Co, Ni)-MOF/ $\text{WO}_3/\text{W}$  thin films. AFM images and the corresponding height profiles of (e)  $\text{WO}_3/\text{W}$  and (f) (Co, Ni)-MOF/ $\text{WO}_3/\text{W}$  photoanode thin films. (g) Tridimensional BFDH morphology of (Co, Ni)-MOF, and the crystal structure of the (200) lattice plane of Co-MOF, Ni-MOF, and (Co, Ni)-MOF. (h) EDS images of (Co, Ni)-MOF/ $\text{WO}_3/\text{W}$  thin film.

assembled from nanoplate covered on the  $\text{WO}_3/\text{W}$  thin film, which is much different from the reported (Co, Ni)-MOF with a nano-parallelepiped-like morphology covered on the nanoporous  $\text{BiVO}_4$  substrate [43]. In contrast with the morphology of Co-MOF, (Co, Ni)-MOF with a 3D hierarchical flower-like array morphology wouldn't block the optical absorption path and could facilitate the diffusion of reactant ions and the produced gas bubble, which is beneficial for producing more photoinduced charges and improving the kinetic transfer efficiency as well as the OER reaction. Moreover, the thickness of the nanoplate assigned to flower-like (Co, Ni)-MOF is about 50–100 nm, which is equivalent to 50–100 coordination structural layers according to the theoretical thickness of (200) crystallographic plane of (Co, Ni)-MOF (Fig. S6). AFM was employed to further identify the height of the (Co, Ni)-MOF/ $\text{WO}_3/\text{W}$  and  $\text{WO}_3/\text{W}$  thin films. From Fig. 2e, it is observed that the  $\text{WO}_3/\text{W}$  has a uniform coral-like nanostructure with a

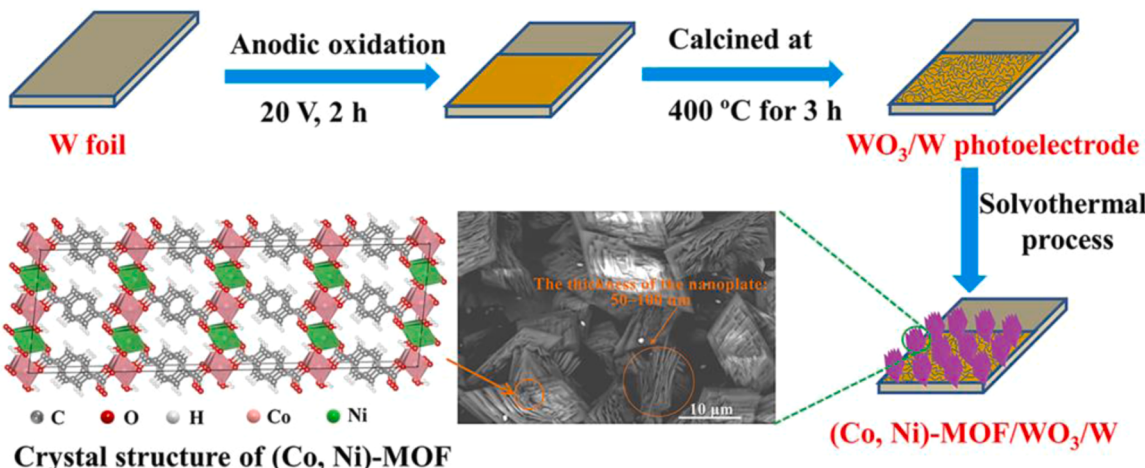
thickness of ~500 nm, which is well-aligned with the SEM images above. Moreover, these findings show that the metal W substrate and the coral-like  $\text{WO}_3$  layer interacted vigorously, reducing the Schottky contact between the metal W substrate and the  $\text{WO}_3$  thin film [53]. The phase diagram is employed to make up for the lack of a shape diagram by providing the surface details when there is too much undulation in the shape diagram. As illustrated in Fig. 2f, a 3D flower-like (Co, Ni)-MOF array with a thickness of ~5  $\mu\text{m}$  consisting of nanoplates covering the entire  $\text{WO}_3/\text{W}$  substrate is clearly presented. Furthermore, the (Co, Ni)-MOF appears to have a two-dimensional (2D) plate-like morphology (Fig. 2g), according to the predicted BFDH crystal morphology. The similar BFDH morphology of Co-MOF and Ni-MOF are displayed in Fig. S7. The largest exposed plane should be assigned to the (200) plane attributed to the strongest XRD peak in Fig. S3, which is equivalent to the tight packing layers of the metal atoms. The exact

configuration of metal atoms on the largest exposed (200) planes of Co-MOF, Ni-MOF, and (Co, Ni)-MOF is illustrated in Fig. 2g, which shows a wealth of coordinatively unsaturated sites on the exposed (200) planes. From Fig. 2h, the EDS mapping analysis confirms the presence of C, O, Co, Ni, and W elements, indicating the flower-like (Co, Ni)-MOF array has been effectively deposited onto the surface of the  $\text{WO}_3/\text{W}$  thin film. Anyway, the EDS mapping result is in accordance with the survey XPS results (Fig. S4a). In addition, Brunauer–Emmett–Teller (BET) specific surface areas of the prepared Co-MOF, Ni-MOF, and (Co, Ni)-MOF powders were measured and given in Fig. S8. It is found that the BET-specific surface area of (Co, Ni)-MOF ( $205.1 \text{ m}^2 \text{ g}^{-1}$ ) falls in between Co-MOF ( $191.4 \text{ m}^2 \text{ g}^{-1}$ ) and Ni-MOF ( $212.8 \text{ m}^2 \text{ g}^{-1}$ ), which might be associated with the morphological features, as shown in Fig. 2.

Herein, the formation mechanism of (Co, Ni)-MOF/ $\text{WO}_3/\text{W}$  photoanode thin film was proposed, as shown in Scheme 1. First of all, a coral-like  $\text{WO}_3/\text{W}$  thin film was synthesized from pure W substrates by anode oxidation reactions. We used a typical two-electrode setup to anodize the W foil, and an  $\text{NH}_4\text{F}$  aqueous acidic solution was employed as the electrolyte, in which soluble fluoride complexes were formed through the chemical dissolution of the tungsten oxide by the  $\text{F}^-$  anion during the anodic oxidation process [54]. Then, an equilibrium is easily reached between oxidation and dissolution with a constant current [55]. After post-calcination treatment, the pre-produced tungsten oxide product from the equilibrium process was crystallized and transformed into a coral-like  $\text{WO}_3$  thin film on the substrate of W foil. Subsequently, a facile solvothermal method was used to deposit the (Co, Ni)-MOF thin film with flower-like morphology on the coral-like  $\text{WO}_3/\text{W}$  thin film. During the formation of a flower-like (Co, Ni)-MOF array, the raw chemicals of  $\text{CoCl}_2 \cdot 6 \text{ H}_2\text{O}$  and  $\text{Ni}(\text{NO}_3)_2 \cdot 6 \text{ H}_2\text{O}$  were hydrolyzed due to the presence of deionized water, resulting in the  $\text{Co}^{2+}$  and  $\text{Ni}^{2+}$  ions were released into the homogeneous solution, which could involve in the coordination reaction with oxygen atoms of terephthalic acid ligands to form the crystalline framework of (Co, Ni)-MOF [56]. Additionally, the nucleation and growth processes of flower-like (Co, Ni)-MOF array under solvothermal treatment may be significantly influenced by ethanol, which might serve as a structure-directing agent that would promote the self-assembly process of (Co, Ni)-MOF nanoplates and result in the formation of flower-like microstructure, as confirmed as follows. The corresponding crystal structure of (Co, Ni)-MOF linked via terephthalate ligands reveals that six O atoms act as the octahedrally coordinated Co and Ni atoms and these pseudo octahedra are further edge/corner coupled with one another in the (200) crystal plane to form the 2D bimetal layers that are separated by terephthalate molecules [57]. In addition, the crystal structures of Co-MOF and Ni-MOF linked via terephthalate ligands and monoclinic phase of  $\text{WO}_3$  are displayed in Fig. S9.

### 3.2. PEC properties and charge transport behavior

The PEC properties of the as-prepared various photoanodes were measured under AM 1.5 G irradiation at  $100 \text{ mW cm}^{-2}$  in the  $0.5 \text{ M Na}_2\text{SO}_4$  solution. The cyclic voltammogram (CV) curves exhibit minimal change when the scan rate increases from  $0.01$  to  $0.05 \text{ V s}^{-1}$  except for a tiny shift in peak locations (Fig. S10a), indicating a larger amount of charges can be stored in the (Co, Ni)-MOF/ $\text{WO}_3/\text{W}$  photoanode. Moreover, the electrochemical double-layer capacitance ( $C_{dl}$ ) measured from the scan-rate dependent CV plots for the (Co, Ni)-MOF/ $\text{WO}_3/\text{W}$  photoanodes is  $74.6 \text{ mF}$  (Fig. S10b). Fig. 3a shows the LSV curves of the as-prepared photoanodes. It is noted that the as-prepared Co-MOF/ $\text{WO}_3/\text{W}$ , Ni-MOF/ $\text{WO}_3/\text{W}$ , and (Co, Ni)-MOF/ $\text{WO}_3/\text{W}$  photoanodes show strong negative shifts in the photocurrent onset potential compared with bare  $\text{WO}_3/\text{W}$  photoanode. Especially, the (Co, Ni)-MOF/ $\text{WO}_3/\text{W}$  photoanode illustrates an ultralow onset potential ( $0.46 \text{ V}$  vs. RHE) compared with bare  $\text{WO}_3/\text{W}$  photoanode ( $0.81 \text{ V}$  vs. RHE), indicating that (Co, Ni)-MOF modified  $\text{WO}_3/\text{W}$  photoanode possesses a larger driving force for water oxidation. The ultralow onset potential could boost the energy conversion efficiency and facilitate the practical application [57]. Moreover, the  $\text{WO}_3/\text{W}$  photoanode shows a  $0.39 \text{ mA cm}^{-2}$  photocurrent at  $1.23 \text{ V}$  vs. RHE, while the photocurrent density of (Co, Ni)-MOF/ $\text{WO}_3/\text{W}$  photoanode reaches ca.  $2.96 \text{ mA cm}^{-2}$  at  $1.23 \text{ V}$  vs. RHE, which is almost 7.6 times greater than that of the  $\text{WO}_3/\text{W}$  photoanode. It means that the (Co, Ni)-MOF/ $\text{WO}_3/\text{W}$  photoanode suppressed the electron-hole recombination process of the PEC reaction and increased the effective electron mobility, leading to enhanced PEC properties. According to the literature, the photocurrent density of (Co, Ni)-MOF/ $\text{WO}_3/\text{W}$  photoanode in this work exceeds most of the reported  $\text{WO}_3$ -based photoanodes deposited with various co-catalysts (Table S2). It is noted that the LSV curves of the  $\text{WO}_3/\text{W}$  samples decorated with Co-MOF, Ni-MOF, and (Co, Ni)-MOF seem to exhibit a "turn-on" voltage around  $1.0 \text{ V}$  vs. RHE, which could be attributed to the dramatically increased charge transfer efficiency and accelerated reaction kinetics from that applied bias [14]. An oxidation peak for Ni-MOF/ $\text{WO}_3/\text{W}$  appeared around  $1.2 \text{ V}$  vs. RHE could be related to the oxidation transformation from  $\text{NiO}_6$  inside the Ni-MOF structure to  $\text{NiO}_6/\text{NiOOH}$  [58]. Additionally, the (Co, Ni)-MOF/ $\text{WO}_3/\text{W}$  photoanode displayed impressively rapid reaction kinetics with a low Tafel slope of  $265 \text{ mV dec}^{-1}$  (Fig. 3b), which is 3.1, 1.5, and 1.02 times lower than those of pure  $\text{WO}_3/\text{W}$ , Co-MOF/ $\text{WO}_3/\text{W}$ , and Ni-MOF/ $\text{WO}_3/\text{W}$ , respectively. Moreover, the effect of atomic ratios of Co to Ni and film thicknesses of the (Co, Ni)-MOF/ $\text{WO}_3/\text{W}$  photoanodes on the photocurrent density was investigated, as illustrated in Fig. 3c derived from the data of Fig. S11. It is found that the photocurrent density is dependent on the atomic ratios of Co to Ni, and the best



Scheme 1. Schematic illustration of the preparation of (Co, Ni)-MOF/ $\text{WO}_3/\text{W}$  photoanode thin film under optimal conditions.

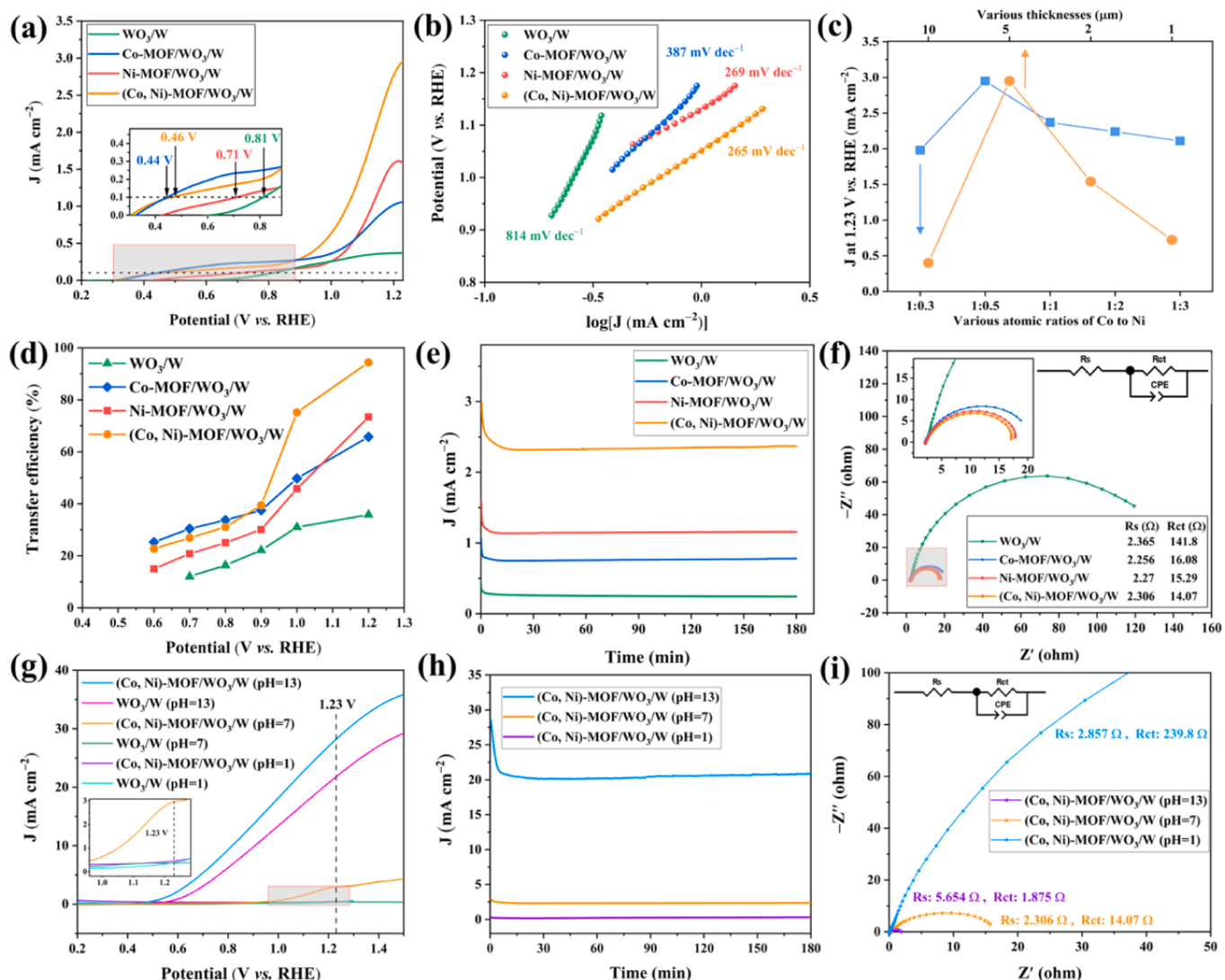


**Fig. 3.** (a) Comparison of LSV curves and (b) Tafel plots of as-prepared  $\text{WO}_3/\text{W}$ , Co-MOF/ $\text{WO}_3/\text{W}$ , Ni-MOF/ $\text{WO}_3/\text{W}$ , and (Co, Ni)-MOF/ $\text{WO}_3/\text{W}$  photoanodes under AM 1.5 G irradiation at 100 mW cm<sup>-2</sup> in the 0.5 M  $\text{Na}_2\text{SO}_4$  solution. (c) Effect of the atomic ratios of Co to Ni and film thicknesses of (Co, Ni)-MOF/ $\text{WO}_3/\text{W}$  photoanodes on the photocurrent at 1.23 V vs. RHE. (d) Charge transfer efficiency versus the potential of the as-prepared photoanodes. (e) The long I-t curves of as-prepared photoanodes. (f) Nyquist plots of EIS (The inset is the enlarged part in the range of 1–20 ohm of  $Z'$ ) of as-prepared various photoanodes with AM 1.5 G. (g) LSV curves of  $\text{WO}_3/\text{W}$  and (Co, Ni)-MOF/ $\text{WO}_3/\text{W}$  photoanodes in various pH-conditions (pH = 1, 7, and 13) under AM 1.5 G irradiation at 100 mW cm<sup>-2</sup>. (h) Stability test of photocurrent density over (Co, Ni)-MOF/ $\text{WO}_3/\text{W}$  photoanode in various pH-conditions with AM 1.5 G irradiation at 1.23 V vs. RHE. (i) Nyquist plots of EIS of (Co, Ni)-MOF/ $\text{WO}_3/\text{W}$  photoanode in different pH-conditions.

performance of photocurrent density is presented in the sample of  $(\text{Co}_1, \text{Ni}_{0.5})\text{-MOF}/\text{WO}_3/\text{W}$  photoanode. Furthermore, the film thickness of the optimal  $(\text{Co}_1, \text{Ni}_{0.5})\text{-MOF}/\text{WO}_3/\text{W}$  photoanode was regulated by adjusting the concentration of the raw chemical materials of  $\text{CoCl}_2 \cdot 6\text{H}_2\text{O}$  and  $\text{Ni}(\text{NO}_3)_2 \cdot 6\text{H}_2\text{O}$  in the mixture solution during the hydrothermal process. The estimated film thickness of the photoanodes for the  $(\text{Co}_1, \text{Ni}_{0.5})\text{-MOF}/\text{WO}_3/\text{W}-1$ ,  $(\text{Co}_1, \text{Ni}_{0.5})\text{-MOF}/\text{WO}_3/\text{W}-2$ ,  $(\text{Co}_1, \text{Ni}_{0.5})\text{-MOF}/\text{WO}_3/\text{W}-3$ , and  $(\text{Co}_1, \text{Ni}_{0.5})\text{-MOF}/\text{WO}_3/\text{W}-4$  was ca. 10, 5, 2, and 1  $\mu\text{m}$ , respectively. It is found that the  $(\text{Co}_1, \text{Ni}_{0.5})\text{-MOF}/\text{WO}_3/\text{W}-2$  photoanode with film thicknesses of ca. 5  $\mu\text{m}$  exhibits the highest photocurrent density at 1.23 V vs. RHE. According to these findings, when film thickness of  $(\text{Co}_1, \text{Ni}_{0.5})\text{-MOF}/\text{WO}_3/\text{W}$  photoanode grows, the photocurrent density first rises and subsequently falls. The following factors may be responsible for the first rise in photocurrent density in PEC characteristics with increasing thickness [59]. (1) an increase in the film thickness means the massive introduction of  $(\text{Co}_1, \text{Ni}_{0.5})\text{-MOF}$ , which produces more surface roughness and increases the surface area available for redox reactions, increasing photocurrent and decreasing

recombination losses; (2) an increase in the film thickness of  $(\text{Co}_1, \text{Ni}_{0.5})\text{-MOF}$  could absorb more visible light (Fig. S12), which increases the generation of photoexcited charge carriers and consequently boosts the photocurrent. However, when the thickness of the thin film increases to 10  $\mu\text{m}$  for  $(\text{Co}_1, \text{Ni}_{0.5})\text{-MOF}/\text{WO}_3/\text{W}-1$ , the photocurrent density starts to decline. This might be because the photogenerated charges may have to travel a longer distance during the transport process, which could result in significant recombination losses. In addition, it is noted that the thickness of the (Co, Ni)-MOF layer ( $\sim 5 \mu\text{m}$ ) on the  $\text{WO}_3/\text{W}$  thin films in this work is far beyond that of the reported common Co/Ni co-catalysts layer ( $\sim 3\text{--}30 \text{ nm}$ ) coating on the semiconductor photoanodes [60,61]. This is because (Co, Ni)-MOF acts not only as a co-catalyst for  $\text{WO}_3/\text{W}$  photoanode but only as an electrocatalyst for OER reaction during the PEC water splitting process, which is much different from the previously reported semiconductor photoanodes decorated by Co/Ni co-catalysts layer [62,63]. In the PEC water splitting system, except for solar light illumination conditions, an external electrical bias was used to control the hole migration for electrocatalytic

OER reaction [64,65]. It was reported that the bimetal (Co, Ni)-MOF itself possessed excellent electrocatalytic OER activity and sustained stability due to the coupling effect between Co and Ni ions [57,66–69]. Therefore, the maximum photocurrent density of (Co, Ni)-MOF/WO<sub>3</sub>/W photoanode with a thickness of ~5 μm is a result of the combination of solar light-driven photocatalysis and external applied bias-driven electrocatalysis at 1.23 V vs. RHE. Moreover, micron-scale thin film is favorably formed for the 3D flower-like (Co, Ni)-MOF array architecture assembled from 2D nanoplate on the substrate of coral-like WO<sub>3</sub>/W thin film in this work, which could resolve the issues of inherent restacking and low yield of 2D MOFs with nanosheets, which is beneficial to the rapid ion diffusion, effective charge transfer and increased exposed active sites for PEC water splitting [34]. Furthermore, a micron-scale (Co, Ni)-MOF array could increase the optical absorption ability in the visible light range (Fig. S12), which means more photoinduced charges would be produced to participate in the PEC water splitting. Such a thick (Co, Ni)-MOF layer might suppress the collapse of the WO<sub>3</sub> electrode, which is attributed to the 3D flower-like (Co, Ni)-MOF array architecture as a protective layer grown on the coral-like WO<sub>3</sub>/W thin film. In addition, 3D hierarchical MOF thin films with micron-scale thickness were reported for OER catalysts [66,70].

To reveal the charge-separation efficiency, transient photocurrent responses at different applied potentials under chopped AM 1.5 G illumination were measured, as depicted in Fig. S13. Because of surface charge recombination, it exhibits a characteristic decrease during the illumination duration from a "spike" to a steady state. The competition between the  $k_{\text{rec}}$  and the  $k_{\text{tr}}$  determines the  $\eta_{\text{trans}}$  of the carrier flow into the surface involved in the OER or HER process, and the calculated  $\eta_{\text{trans}}$  is illustrated in Fig. 3d. It is noteworthy that (Co, Ni)-MOF/WO<sub>3</sub>/W photoanode exhibits the highest charge-transfer efficiency in an applied bias of 0.9–1.2 V among these as-prepared photoanodes, indicating superior charge separation ability, which might result from the (Co, Ni)-MOF could function as an efficient hole storage layer for the capture and accumulation of photogenerated holes from WO<sub>3</sub>/W [71]. Long-term photocurrent-time (I-t) measurements were conducted at a constant potential of 1.23 V vs. RHE for 180 min to identify the stability of the (Co, Ni)-MOF/WO<sub>3</sub>/W photoanode. As seen in Fig. 3e, all photoanode thin films exhibit a stable current density for the period of 3 h, indicating their outstanding PEC stability in the neutral electrolyte. Moreover, the excellent PEC stability means the chemical dissolution of the general WO<sub>3</sub> thin films in the neutral electrolyte was absent in our cases, facilitating the practical PEC application because the majority of PEC conditions in practice are closer to the neutral solution [21]. In addition, XRD patterns, FTIR, and XPS spectra of (Co, Ni)-MOF/WO<sub>3</sub>/W thin film after PEC water splitting were measured, as shown in Fig. S14. It is found that there is almost no obvious change for the crystal as well as molecular structures of (Co, Ni)-MOF and chemical bonding states of W, Co, and Ni elements in (Co, Ni)-MOF/WO<sub>3</sub>/W thin film after PEC water splitting. Besides, the PEC performance of WO<sub>3</sub>/W and traditional WO<sub>3</sub>/FTO substrates is compared. As shown in Fig. S15a, the WO<sub>3</sub>/W photoanode shows significantly higher photocurrent density in the 0.5 M Na<sub>2</sub>SO<sub>4</sub> solution compared with WO<sub>3</sub>/FTO substrate, which might be resulting from the outstanding electroconductivity of metal W foils compared with that of FTO coated glasses and the Schottky junction in the WO<sub>3</sub>/W photoanode, facilitating the effective electron transport from WO<sub>3</sub> efficient electron transport from WO<sub>3</sub> catalysts in the direction of the conductive W foils, where the Schottky barrier stops electron prevents electrons from returning [48,72]. Moreover, (Co, Ni)-MOF/WO<sub>3</sub>/W photoanode exhibits significantly higher photocurrent density than (Co, Ni)-MOF/WO<sub>3</sub>/FTO, especially in the applied bias of 1.0–1.23 V, indicating the greatly enhanced OER activity. The EIS Nyquist plots demonstrate that the WO<sub>3</sub> and (Co, Ni)-MOF/WO<sub>3</sub> on the W foils exhibit greatly lower electron transfer resistance compared with that on the FTO-coated glasses (Fig. S15b), further confirming the highly efficient electron transport ability of WO<sub>3</sub> and (Co, Ni)-MOF/WO<sub>3</sub> on the W foils. These results demonstrate that WO<sub>3</sub>/W as a substrate is a good

choice for the WO<sub>3</sub>-based photoanodes.

A semicircular Nyquist EIS plot diameter was compared. By using Zview software, equivalent circuits were constructed to assess the electron transfer resistance ( $R_{\text{ct}}$ ) between the photoanode and electrolyte at the interface, lower  $R_{\text{ct}}$  is associated with smaller arc radii [43]. As illustrated in Fig. 3f, the bare WO<sub>3</sub>/W photoanode exhibits a large hemicycle under AM 1.5 G irradiation. It indicates that WO<sub>3</sub>/W photoanodes have a high charge transfer barrier at their interface. The fitting results show that the  $R_{\text{ct}}$  of Co-MOF/WO<sub>3</sub>/W (15.29 Ω), Ni-MOF/WO<sub>3</sub>/W (16.08 Ω), and (Co, Ni)-MOF/WO<sub>3</sub>/W (14.06 Ω) are considerably lower than that of WO<sub>3</sub>/W (141.8 Ω), further ascertaining the promotion of the charge transfer by Co-MOF, Ni-MOF, and (Co, Ni)-MOF across the electrolyte/semiconductor interface. Among these as-prepared photoanodes, the (Co, Ni)-MOF/WO<sub>3</sub>/W photoanode shows the lowest  $R_{\text{ct}}$ , indicating that (Co, Ni)-MOF/WO<sub>3</sub>/W exhibits the fastest transfer rate of photogenerated charges. By growing flower-like (Co, Ni)-MOF directly on the WO<sub>3</sub>/W conductive substrate, the continuous contact between MOF catalysts and conductive substrates might assure quick charge transfer and avoid the shedding of catalysts [34]. As a means of determining the type of semiconductor material and the flat-band potentials ( $E_{\text{fb}}$ ), the Mott-Schottky plots were measured and the results were displayed in Fig. S16. According to the evaluation, the  $E_{\text{fb}}$  of WO<sub>3</sub>/W, Co-MOF/WO<sub>3</sub>/W, Ni-MOF/WO<sub>3</sub>/W, and (Co, Ni)-MOF/WO<sub>3</sub>/W photoanodes is 1.36, 1.35, 1.38, and 1.43 V vs. RHE, respectively, which is very close to each other. Moreover, the four curves' observed positive slopes imply that all photoanode thin films are composed of n-type semiconductors. It is also noted that the slope of the curve of (Co, Ni)-MOF/WO<sub>3</sub>/W photoanode is smaller compared with that of Ni-MOF/WO<sub>3</sub>/W, Co-MOF/WO<sub>3</sub>/W, and WO<sub>3</sub>/W photoanodes, indicating that its carrier concentration is larger, which is more beneficial for photoelectrochemical water splitting because the slopes and the charge carrier density have an inverse relationship [73]. Contact angle measurement was performed to assess the water wettability of the as-prepared photoanode thin films (Fig. S17). It indicates that the (Co, Ni)-MOF/WO<sub>3</sub>/W thin film displays higher hydrophilicity than the WO<sub>3</sub>/W thin film. Compared with that of WO<sub>3</sub>/W, the higher hydrophilicity of (Co, Ni)-MOF/WO<sub>3</sub>/W can be associated with the -OH groups and -COO<sup>-</sup> of terephthalate anions in the (Co, Ni)-MOF as confirmed by FTIR spectra above. Due to the high hydrophilicity of (Co, Ni)-MOF/WO<sub>3</sub>/W photoanode, its surface could readily adsorb water molecules, which is advantageous to the PEC water splitting efficiency.

To study the influence of pH values on the as-prepared photoanodes, PEC tests were also performed in various electrolytes, including 0.1 M H<sub>2</sub>SO<sub>4</sub> solution (pH = 1) with a calomel electrode serving as the reference electrode and 0.1 M KOH solution (pH = 13) with a Hg/HgO reference electrode. As shown in Fig. 3g, the LSV curves for WO<sub>3</sub>/W and (Co, Ni)-MOF/WO<sub>3</sub>/W photoanodes in different electrolytes are compared, where the pH values are 1 (0.1 M H<sub>2</sub>SO<sub>4</sub>), 7 (0.5 M Na<sub>2</sub>SO<sub>4</sub>), and 13 (0.1 M KOH), respectively. It illustrates that both WO<sub>3</sub>/W and (Co, Ni)-MOF/WO<sub>3</sub>/W photoanodes exhibit extraordinary photocurrent densities at pH = 13 in the alkaline condition, which are much higher than that at pH = 7 and pH = 1. Especially, the (Co, Ni)-MOF/WO<sub>3</sub>/W photoanode achieves the highest photocurrent density at 1.23 V vs. RHE, which reaches 28.3 mA cm<sup>-2</sup>. Turnover frequency (TOF) is defined as the number of conversions per unit of catalytic active sites of the reactant molecule [34], which could be estimated by the following standard Eq. (6) [74].

$$\text{TOF} = \frac{J \times A}{4 \times F \times m} \quad (6)$$

where  $J$  is the current density (A cm<sup>-2</sup>) at an overpotential of 0.27 V,  $A$  (cm<sup>2</sup>) is the area of the electrode,  $m$  (mol) is the number of moles of the active materials placed on the electrode, and  $F$  is the Faraday constant (96485 C mol<sup>-1</sup>). Based on the current density of (Co, Ni)-MOF/WO<sub>3</sub>/W photoanode in 0.1 M KOH solution (Fig. 3g), TOF was calculated according to Eq. (6). It is found that the calculated TOF of (Co, Ni)-MOF on

the  $\text{WO}_3/\text{W}$  photoanode in 0.1 M KOH solution is  $0.038 \text{ s}^{-1}$ , which is higher than that of the reported  $\text{CoOOH}$  ( $0.01 \text{ s}^{-1}$ ) and  $\text{NiOOH}$  ( $0.00028 \text{ s}^{-1}$ ) under alkaline condition [75,76]. This might be due to the more exposed active sites attributed to the coordinated unsaturated Co and Ni metal atoms in the 3D flower-like (Co, Ni)-MOF array architecture.

Moreover, the stability of photocurrent density over (Co, Ni)-MOF/ $\text{WO}_3/\text{W}$  photoanode in various pH-conditions with AM 1.5 G irradiation at 1.23 V vs. RHE are examined, as illustrated in Fig. 3h. It demonstrates (Co, Ni)-MOF/ $\text{WO}_3/\text{W}$  photoanode maintains more than ca. 75 % of its starting value at 1.23 V vs. RHE under AM 1.5 G irradiation during a 3-hour operation in various electrolytes, suggesting that (Co, Ni)-MOF/ $\text{WO}_3/\text{W}$  photoanode permits pH-independent OER. Furthermore, the semicircular Nyquist EIS plot diameter of (Co, Ni)-MOF/ $\text{WO}_3/\text{W}$  photoanode under various electrolytes was compared, as displayed in Fig. 3i. It is found that the  $R_{\text{ct}}$  of (Co, Ni)-MOF/ $\text{WO}_3/\text{W}$  photoanode in the alkaline condition is much smaller than that in the neutral and acidic conditions, indicating a significantly decreased electron transfer resistance in the alkaline condition, which is consistent with the LSV results.

The relationship between light harvesting and the photocurrent density of as-prepared various photoanodes was further identified by the wavelength-dependent IPCE measurements, as depicted in Fig. 4a. Apparently, the deposition of Co-MOF, Ni-MOF, and (Co, Ni)-MOF onto the substrate of  $\text{WO}_3/\text{W}$  results in a remarkable increase in IPCE in the 350–450 nm spectral range. Moreover, the (Co, Ni)-MOF/ $\text{WO}_3/\text{W}$  photoanode displays the highest IPCE of 82.3 % at 360 nm in the UV region and 75.3 % at 400 nm in the visible light range, which exhibits an improvement of 57.1 % and 53.3 % in the corresponding region compared with bare  $\text{WO}_3/\text{W}$  photoanode (25.2 % and 22.0 %). Such a

high IPCE value for (Co, Ni)-MOF/ $\text{WO}_3/\text{W}$  photoanode exceeds the most of previously reported  $\text{WO}_3$ -based photoanodes (Table S2). Furthermore, it is observed that the onset of IPCE profiles appeared at ca. 440 nm for the as-prepared various photoanodes, which is close to the absorbance edge of their UV-Vis absorption spectra (Fig. 1f). Additionally, ABPE was calculated to determine the half-cell solar to energy conversion efficiency assuming 100 % Faradaic efficiency [77,78], as illustrated in Fig. 4b. It is found that the maximum ABPE of (Co, Ni)-MOF/ $\text{WO}_3/\text{W}$  photoanode reaches 0.22 % at 1.07 V vs. RHE under AM 1.5 G solar spectrum, which is about 3.3 times larger than that of bare  $\text{WO}_3/\text{W}$  photoanode (0.066 % at 0.93 V vs. RHE). Moreover, the calculated maximum ABPE values of Co-MOF/ $\text{WO}_3/\text{W}$  (0.08 % at 1.10 V vs. RHE) and Ni-MOF/ $\text{WO}_3/\text{W}$  (0.14 % at 1.07 V vs. RHE) are also greater than that of pure  $\text{WO}_3/\text{W}$  photoanode. Anyway, these results demonstrate that the deposition of Co-MOF, Ni-MOF, and (Co, Ni)-MOF onto the substrate of  $\text{WO}_3/\text{W}$  could boost the solar to electrochemical energy conversion efficiency significantly. Fig. 4c shows the  $\text{H}_2$  and  $\text{O}_2$  evolution rates of the as-prepared various photoanodes with an applied potential of 1.23 V vs. RHE under AM 1.5 G irradiation. It reveals that the molar ratio of the evolved  $\text{H}_2$  and  $\text{O}_2$  is nearly 2:1, indicating the simultaneous generation of  $\text{H}_2$  and  $\text{O}_2$  from the photoelectrochemical water splitting. Also, it is noticed that all the Co-MOF, Ni-MOF, and (Co, Ni)-MOF modified  $\text{WO}_3/\text{W}$  photoanodes exhibit higher PEC properties for water splitting than bare  $\text{WO}_3/\text{W}$  photoanode, in which the (Co, Ni)-MOF/ $\text{WO}_3/\text{W}$  photoanode reveals the highest activity (48.7 and 23.6  $\mu\text{mol cm}^{-2} \text{ h}^{-1}$  for evolved  $\text{H}_2$  and  $\text{O}_2$ , respectively). Moreover, the Faradaic efficiency (FE) of (Co, Ni)-MOF/ $\text{WO}_3/\text{W}$  photoanode is determined to 90.07 %, which is 1.5 times higher than that of  $\text{WO}_3/\text{W}$  photoanode (60.5 %). Furthermore, STH efficiency was calculated to

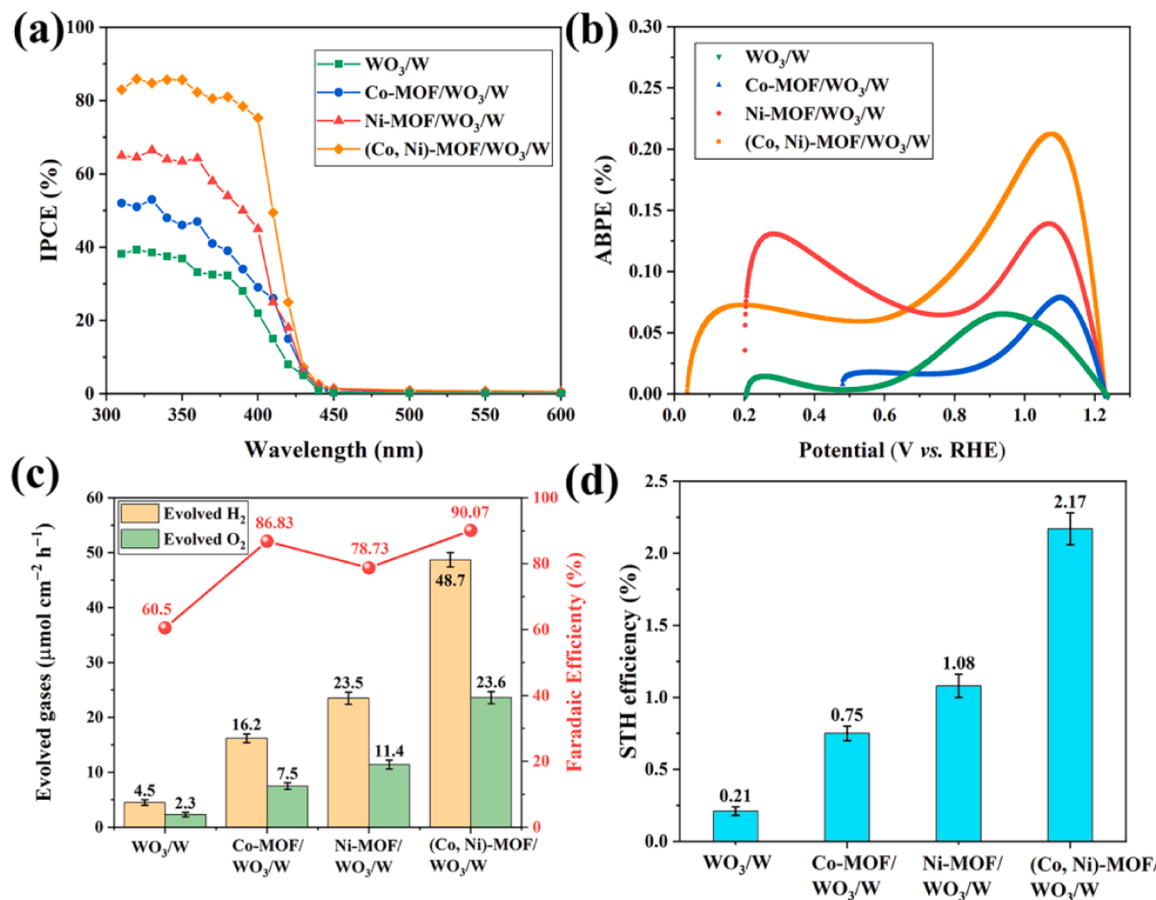


**Fig. 4.** (a) IPCE, (b) ABPE, (c)  $\text{H}_2$  and  $\text{O}_2$  evolution efficiency as well as Faradaic efficiency, and (d) STH efficiency of the as-prepared various photoanodes measured at a constant potential of 1.23 V vs. RHE in the 0.5 M  $\text{Na}_2\text{SO}_4$  solution under AM 1.5 G irradiation.

examine the overall STH efficiency, as illustrated in Fig. 4d. It is found that the calculated STH efficiency of  $\text{WO}_3/\text{W}$ , Co-MOF/ $\text{WO}_3/\text{W}$ , Ni-MOF/ $\text{WO}_3/\text{W}$ , and (Co, Ni)-MOF/ $\text{WO}_3/\text{W}$  photoanodes is 0.21 %, 0.75 %, 1.08 %, and 2.17 %, respectively. Apparently, a 10.3-fold increase of STH efficiency was recorded in (Co, Ni)-MOF/ $\text{WO}_3/\text{W}$  photoanode than that of bare  $\text{WO}_3/\text{W}$  photoanode. Therefore, it further indicates that (Co, Ni)-MOF/ $\text{WO}_3/\text{W}$  photoanode has a bright future for converting solar energy.

To gain a comprehensive understanding of the separation behavior and spatial distribution of photogenerated charges, photo-assisted KPFM of (Co, Ni)-MOF/ $\text{WO}_3/\text{W}$  and  $\text{WO}_3/\text{W}$  was utilized to record the surface potential images and curves of the samples under both dark and bright conditions, as shown in Fig. 5a–f. It is found that the surface potential difference of (Co, Ni)-MOF/ $\text{WO}_3/\text{W}$  is much higher in the dark (59.4 mV) than that for  $\text{WO}_3/\text{W}$  (22.1 mV). This suggests that the (Co, Ni)-MOF array loaded onto the surface of the  $\text{WO}_3/\text{W}$  photoanode excites a stronger built-in electric field, which is consistent with the following DFT results. Moreover, both the samples of (Co, Ni)-MOF/ $\text{WO}_3/\text{W}$  and  $\text{WO}_3/\text{W}$  show higher surface potentials when illuminated than when they are dark. It is found that the surface potential of  $\text{WO}_3/\text{W}$

under light rises by just 38.5 mV relative to that under darkness. On the contrary, the surface potential of (Co, Ni)-MOF/ $\text{WO}_3/\text{W}$  rises by 88.9 mV after illumination compared with that in darkness. These findings unequivocally demonstrate that, in response to light excitation, more photogenerated holes collect on the surface of (Co, Ni)-MOF/ $\text{WO}_3/\text{W}$ ; in other words, photogenerated holes tend to congregate on (Co, Ni)-MOF arrays. It indicates that (Co, Ni)-MOF promotes the production and separation of photogenerated carriers. The conclusion of the accumulation of photogenerated holes by comparing the surface potential difference using photo-assisted KPFM was also demonstrated in the literature [79]. Furthermore, the separation and transfer paths of photogenerated charges for (Co, Ni)-MOF/ $\text{WO}_3/\text{W}$  photoanode are discussed based on the above photo-assisted KPFM and energy band positions of  $\text{WO}_3$  and (Co, Ni)-MOF. As illustrated in Fig. S18a and b, the band gaps of  $\text{WO}_3$  and (Co, Ni)-MOF are 2.64 and 2.61 eV according to their Tauc plots, respectively. The CB positions of  $\text{WO}_3$  and (Co, Ni)-MOF are estimated from Mott–Schottky plots (Fig. S18c), which are determined to be 0.49 and –0.29 V, respectively. Thus, the VB levels of  $\text{WO}_3$  and (Co, Ni)-MOF are determined to be 3.13 and 2.32 V, respectively. Therefore, the corresponding energy band positions of  $\text{WO}_3$  and

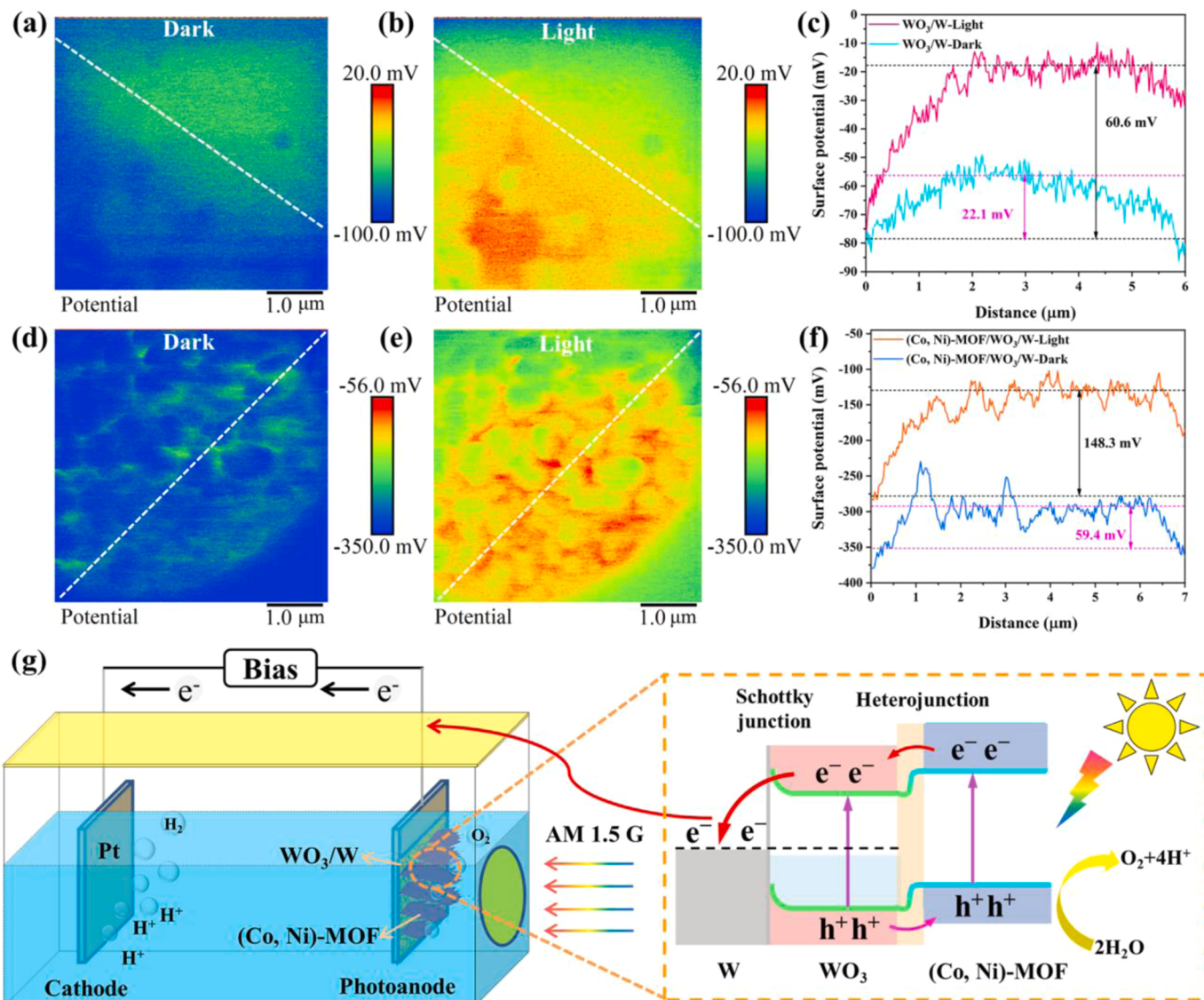


**Fig. 5.** KPFM potential images and the corresponding surface potential curves along the line in the dark and under illumination for (a–c)  $\text{WO}_3/\text{W}$  and (d–f) (Co, Ni)-MOF/ $\text{WO}_3/\text{W}$ . (g) The schematic illustration of separation and transfer paths of photogenerated charges for (Co, Ni)-MOF/ $\text{WO}_3/\text{W}$  photoanode during the PEC process.

(Co, Ni)-MOF are illustrated in Fig. S18d. Upon AM 1.5 G irradiation, both  $\text{WO}_3$  and (Co, Ni)-MOF in the (Co, Ni)-MOF/ $\text{WO}_3$ /W photoanode could be excited to produce photogenerated electrons and holes. The built-in electric field at the heterojunction interface could drive the photogenerated electrons of (Co, Ni)-MOF to move spontaneously to the CB of  $\text{WO}_3$  since the CB level of (Co, Ni)-MOF is higher than that of  $\text{WO}_3$ , and then the photogenerated electrons would transfer across the Schottky junction between  $\text{WO}_3$  and metal W foils to reach the cathode under the applied bias to participate in the hydrogen evolution reaction, while the photogenerated holes tend to flow into the VB of (Co, Ni)-MOF and the accumulated photogenerated holes on the VB of (Co, Ni)-MOF would involve into the OER process, as illustrated in Fig. 5g. Thus, the photogenerated charges are effectively separated and the solar-driven PEC water splitting is significantly improved.

### 3.3. DFT calculations and mechanism analysis

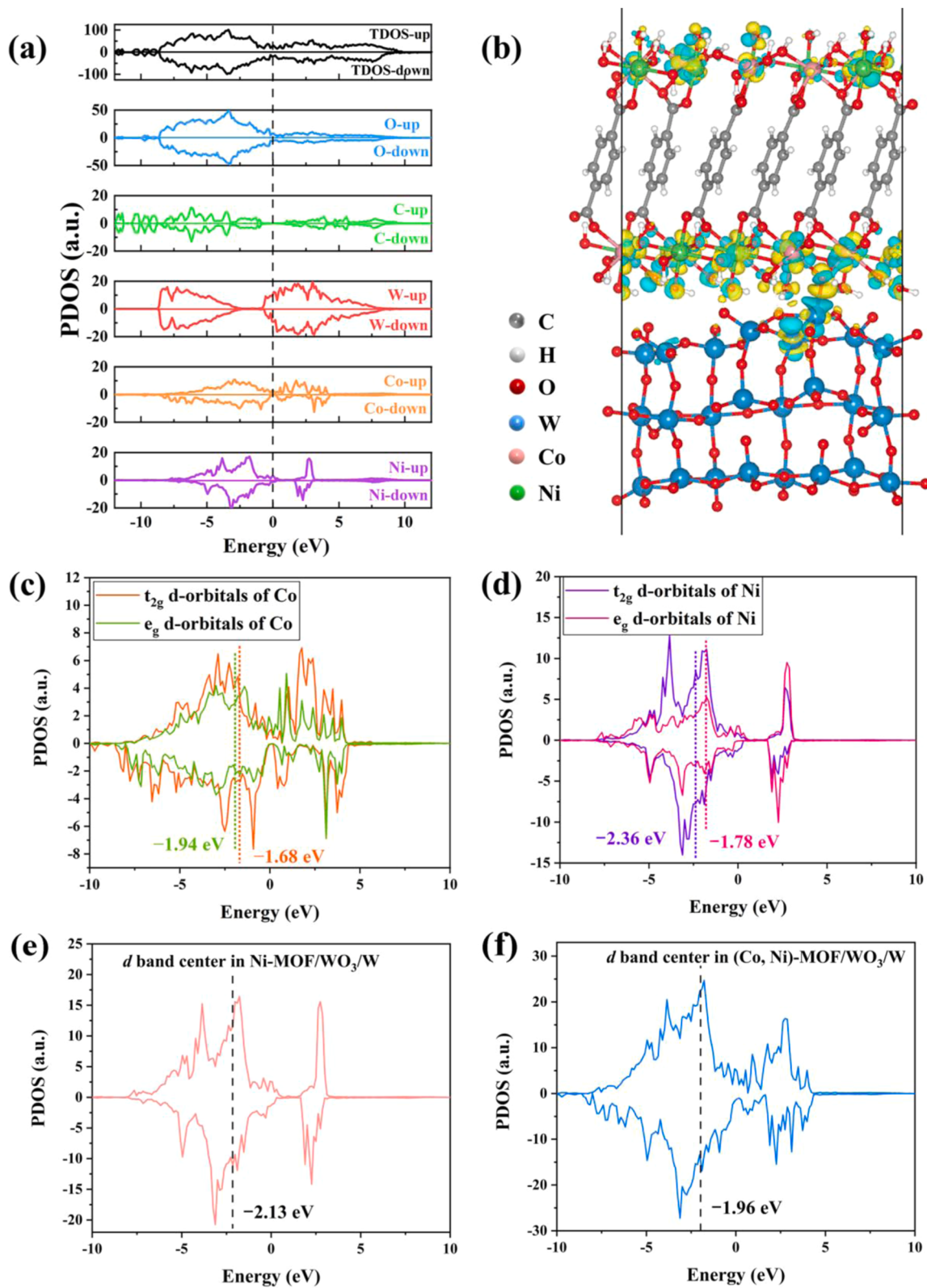
The enhanced PEC performance of (Co, Ni)-MOF/ $\text{WO}_3$ /W photoanode might be attributed to two factors. The first reason is the formation of heterojunction at the (Co, Ni)-MOF and  $\text{WO}_3$  interface, which promotes the separation efficiency of photo-induced electrons and holes by the presence of junction as discussed above. The second reason might be associated with the electronic structure of heterostructure catalysts and the energy barrier of the OER process [80,81]. To have a deeper understanding of the PEC water oxidation process, DFT calculations were conducted to clarify the electronic structure and Gibbs free energies of the OER process.

To mitigate the potential lattice incompatibility between the stacking layers, a specific heterostructure model was employed, as depicted in Fig. S19a. This model consisted of a supercell of (Co, Ni)-MOF (200) with a  $\sqrt{3} \times 5 \times 1$  lattice configuration and a supercell of  $\text{WO}_3$  (200) with a lattice structure of  $1 \times 2 \times 1$ , ensuring that the lattice mismatch remained below 10 %. After undergoing geometric optimization, the interaction between the (Co, Ni)-MOF surface and the  $\text{WO}_3$  surface induces changes in both the (Co, Ni)-MOF and  $\text{WO}_3$  surfaces, as illustrated in Fig. S19b. By considering the equilibrium lattice constant, the spin-polarized partial density of states (PDOS) calculations take into account the most stable and relaxed configuration of the heterostructure, and the results are shown in Fig. 6a. Analyzing the PDOS provides valuable insights into the distribution of electronic states and their respective contributions to the total density of states (TDOS) within the system. The heterostructure model exhibits typical spin gapless semiconductor behavior in the minority spin channel (spin up and down) and potentially enables variable spin transport [82]. It is also found that the O, C, W, Co, and Ni states contribute significantly to the total DOS. In both the spin-up and spin-down channels, the DOS around the Fermi level is primarily determined by the 5d electrons of the high-valence transition-metal W atoms and the 3d electrons of the lower-valence transition-metal Co atoms. However, the 3d electrons of Ni atoms have made little to contribute to the DOS around the Fermi level, which can be attributed to the fact that the energy levels of the 3d states of Ni atoms are considerably distant from the Fermi level, rendering them largely irrelevant in determining the electronic behavior in this energy range. In contrast to Co atoms, it is notable that Ni atoms have fewer empty 3d states above the Fermi level, which may indicate that Ni atoms in the (Co, Ni)-MOF/ $\text{WO}_3$ /W are more active in their interactions with intermediates during the OER process. The differential charge density was calculated to examine the charge redistribution between (Co, Ni)-MOF and  $\text{WO}_3$ , which could be realized from the charge accumulation (yellow) or depletion (cyan) regions at the interface of the heterostructure. As seen in Fig. 6b, the (Co, Ni)-MOF surface at the interface region is primarily dominated by the yellow region with some cyan region partial occupancy, whereas the  $\text{WO}_3$  surface is predominantly filled by the cyan area with some yellow region slight coverage, indicating (Co, Ni)-MOF gains electrons while  $\text{WO}_3$  donates electrons, resulting in

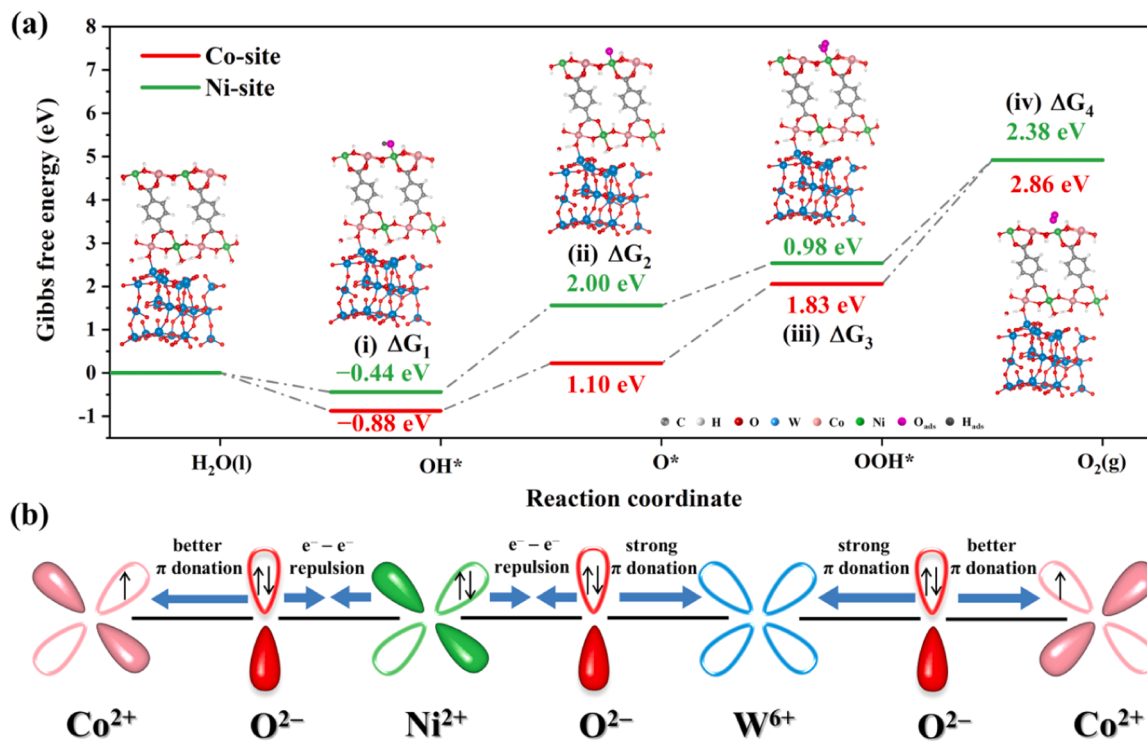
the creation of the internal electric field pointing from and  $\text{WO}_3$  to (Co, Ni)-MOF and the bending of the energy bands at the interface. Additionally, it is noted that the electron density at the W atoms of the  $\text{WO}_3$  surface is decreased greatly while the electron density at the O atoms of the (Co, Ni)-MOF surface is increased significantly, indicating that the free electrons effectively move across the interface from  $\text{WO}_3$  surface to (Co, Ni)-MOF. This outcome demonstrates how the (Co, Ni)-MOF controls the electronic structure of the  $\text{WO}_3$  photoanode and so causes charge redistribution. To comprehend the spin transition, the crystal-field splitting energy of the 3d orbitals was also determined. The  $t_{2g}$  and  $e_g$  centers of Co sites are situated at  $-1.68$  and  $-1.94$  eV with a crystal-field splitting energy of 0.26 eV, while those of Ni centers are situated at  $-2.36$  and  $-1.78$  eV with a crystal-field splitting energy of 0.58 eV, as can be seen in Fig. 6c and d. These findings support the notion that Co sites have a lower crystal-field splitting energy than Ni sites. The theoretical d-band centers in Ni-MOF/ $\text{WO}_3$ /W and (Co, Ni)-MOF/ $\text{WO}_3$ /W were calculated by the DFT method, as illustrated in Fig. 6e and f. It shows that the d-band center in (Co, Ni)-MOF/ $\text{WO}_3$ /W located at  $-1.96$  eV is closer to the Fermi level than that in Ni-MOF/ $\text{WO}_3$ /W at  $-2.13$  eV, indicating that the introduction of Co ions in (Co, Ni)-MOF leads to an upshift of d-band center compared with Ni-MOF. Furthermore, high-resolution VB-XPS was used to realize the d-band center of Ni-MOF/ $\text{WO}_3$ /W and (Co, Ni)-MOF/ $\text{WO}_3$ /W, as shown in Fig. S20. It should be pointed out that the valence band range of 0–6 eV entirely contributed to the d-band of metallic elements since the carbon signal in the valence band emerges over 6 eV [83,84]. It is found that the experimental d-band center from VB-XPS for (Co, Ni)-MOF/ $\text{WO}_3$ /W (2.30 eV) is closer to the Fermi level than that for Ni-MOF/ $\text{WO}_3$ /W (2.82 eV). This result indicates that the same changing trends of the d-band centers appear even though the computed d-band centers from DFT differ from the experimental d-band centers from VB-XPS. Generally,  $\text{H}_2\text{O}$  molecule adsorption is thought to be more advantageous with a higher d-band center [85]. Therefore, it would appear that (Co, Ni)-MOF is advantageous for the adsorption of  $\text{H}_2\text{O}$  molecules for OER compared with Ni-MOF during the PEC process.

Fig. 7a outlines the Gibbs free energy at various reaction steps involved in the OER process over the (Co, Ni)-MOF/ $\text{WO}_3$ /W, including adsorption (step i), dissociation (steps ii and iii), and desorption (step iv), aiding in the understanding of the reaction mechanism and kinetics. It is found that the energy barrier ( $\Delta G_1$ ) for  $\text{OH}^*$  generation at the Co sites ( $-0.88$  eV) is inversely proportional to the adsorption strength of OH, which is substantially lower than that at the Ni sites ( $-0.44$  eV). The lower  $\Delta G_1$  value in the Co sites as compared to the Ni sites indicates preferential energy adsorption of OH and facilitates the initial stage of OER during PEC water splitting. Nevertheless, the inhibited  $\text{O}_2$  desorption is shown by the strong  $\text{OH}^*$  binding to Co sites, which subsequently prevents further water oxidation. Furthermore, this result suggests that the adsorption of OH at the Ni sites has been modified, preventing the electroactive site from being inhibited by the stronger OH adsorption [31].  $\Delta G_2$  indicates the OH radical dissociation of step ii, which has a greater energy barrier on the Ni sites (2.00 eV) than on the Co sites (1.10 eV). Additionally, the over-occupancy of the  $e_g$  orbital is excessively high [86], as seen by the  $\Delta G_3$  values of 1.83 eV at the Co site and 0.98 eV at the Ni site. Besides, it has been determined that the  $\Delta G_4$  values of the Ni and Co sites in (Co, Ni)-MOF/ $\text{WO}_3$ /W are 2.38 eV and 2.86 eV, respectively. Apart from that, the Ni sites are the most advantageous active sites for OER since the theoretical overpotential of Ni sites is 1.15 V, which is substantially lower than that of Co sites (1.63 V), as illustrated in Fig. S21.

The interfacial electronic coupling behavior was addressed in detail to acquire a thorough understanding of how the (Co, Ni)-MOF boosts the PEC activity of the  $\text{WO}_3$ /W photoanode. Because  $\text{Co}^{2+}$  has a high spin state and a  $3d^7$  valence electronic structure, it contains unpaired electrons in the  $\pi$ -symmetry ( $t_{2g}$ ) d-orbitals, which have the potential to interact with the bridging  $\text{O}_2^-$  through  $\pi$ -donation. In contrast, the d-orbitals of  $\text{Ni}^{2+}$  with  $\pi$ -symmetry ( $t_{2g}$ ), which has a valence electronic



**Fig. 6.** (a) The PDOS calculations of a heterostructure model made up of (Co, Ni)-MOF and WO<sub>3</sub>. (b) The calculated differential charge density between (Co, Ni)-MOF and WO<sub>3</sub>. (d) Projected DOS of the t<sub>2g</sub> and e<sub>g</sub> orbitals of the Co and Ni atoms in (Co, Ni)-MOF. Projected DOS of the Ni 3d orbitals in (e) Ni-MOF/WO<sub>3</sub>/W and (f) (Co, Ni)-MOF/WO<sub>3</sub>/W by DFT method.



**Fig. 7.** (a) The OER process on the heterostructure model of the (Co, Ni)-MOF/WO<sub>3</sub> surface as depicted by the Gibbs free energy diagram. (b) The schematic illustration of the electronic interaction between Co<sup>2+</sup>, O<sup>2-</sup>, Ni<sup>2+</sup>, and W<sup>6+</sup> in the (Co, Ni)-MOF.

structure of 3d<sup>8</sup>, are totally occupied. It turns out that the primary interaction between the bridging O<sup>2-</sup> and Ni<sup>2+</sup> is the electron–electron (e<sup>-</sup>–e<sup>-</sup>) repulsion. Following the Ni<sup>2+</sup> and Co<sup>2+</sup> connection, an e<sup>-</sup>–e<sup>-</sup> repulsion exists between O<sup>2-</sup> and Ni<sup>2+</sup>, which could enhance the π-donation through Co–O and result in a partial charge transfer from Ni<sup>2+</sup> to Co<sup>2+</sup> [57,87]. As a result of strong π-donation, electrons in Ni<sup>2+</sup> would move to the d-orbitals of W<sup>6+</sup> utilizing O<sup>2-</sup> as an intermediary [88]. In this situation, electron delocalization in the (Co, Ni)-MOF/WO<sub>3</sub>/W photoanode, as illustrated in Fig. 7b, is the result of the electron transport among mixed-valence metal ions with varying degrees of e<sub>g</sub> orbitals filling eventually. The higher carrier filling factor, quicker transfer rate of photogenerated charges, and higher carrier concentration for the (Co, Ni)-MOF/WO<sub>3</sub>/W photoanode as mentioned above are all attributed to the electron delocalization brought on by the coupling effect between Co, Ni, and W ions. These theoretical and practical findings show that it is a powerful method for developing high-performance PEC catalysts by controlling the interactions between Co and Ni atoms in ordered MOF structures on the WO<sub>3</sub>/W photoanode.

#### 4. Conclusions

We have developed a 3D hierarchical flower-like (Co, Ni)-MOF array modified WO<sub>3</sub>/W photoanode for water splitting in the solar-driven PEC system prepared through a facile solvothermal approach. It is found that the (Co, Ni)-MOF/WO<sub>3</sub>/W photoanode exhibits higher hydrophilicity compared with the WO<sub>3</sub>/W photoanode, which facilitates the water molecules' adsorption on the photoanode surface during PEC water splitting. Additionally, the photocurrent of optimal (Co<sub>1</sub>, Ni<sub>0.5</sub>)-MOF/WO<sub>3</sub>/W photoanode with a film thickness of ~5 μm is approximately 7.6 times higher than that of bare WO<sub>3</sub>/W photoanode at 1.23 V vs. RHE for water oxidation in the 0.5 M Na<sub>2</sub>SO<sub>4</sub> solution, reaching 2.96 mA cm<sup>-2</sup>. Furthermore, the highest photocurrent density (Co, Ni)-MOF/WO<sub>3</sub>/W photoanode was obtained in the alkaline electrolyte at 1.23 V vs. RHE, which reaches 28.3 mA cm<sup>-2</sup>. DFT calculations indicate that the free electrons effectively move across the interface from the WO<sub>3</sub> surface to

(Co, Ni)-MOF. Moreover, it has been demonstrated that the Co sites with a higher d-band center have a lower crystal-field splitting energy than Ni sites and exhibit a lower ΔG<sub>1</sub> for OH\* generation during the PEC process, while the Ni sites show a lower theoretical overpotential for OER than Co sites. Therefore, the enhanced PEC water oxidation performance is ascribed to the electron delocalization in the (Co, Ni)-MOF/WO<sub>3</sub>/W photoanode, which is the result of the electron transport among mixed-valence metal ions (Co, Ni, and W ions) with varying degrees of e<sub>g</sub> orbitals filling eventually. Consequently, this work demonstrates that electron delocalization could be used to boost the traditional PEC photoanode performance.

#### CRediT authorship contribution statement

**Xiu-Li Yang:** Writing – original draft, Software, Methodology, Investigation, Data curation. **Lihua Zhang:** Writing – original draft, Methodology, Investigation. **Jinkang Pan:** Writing – original draft, Methodology, Investigation, Formal analysis, Data curation. **Pengyu Dong:** Writing – original draft, Methodology, Investigation, Funding acquisition, Formal analysis, Data curation, Conceptualization. **Ming-Hua Xie:** Writing – review & editing, Supervision, Funding acquisition, Conceptualization. **Jinlong Zhang:** Writing – review & editing, Funding acquisition, Conceptualization.

#### Declaration of Competing Interest

The authors declare that they have no known competing financial interests or personal relationships that could have appeared to influence the work reported in this paper.

#### Data availability

Data will be made available on request.

## Acknowledgments

This work has been funded by the National Key R&D Program of China (2022YFB3803600 and 2022YFE0107900), the National Natural Science Foundation of China (21403184, 22171239, and 21972040), the Qinglan Project of Jiangsu Province, Natural Science Foundation of the Jiangsu Higher Education Institutions of China (22KJA430008), the Natural Science Foundation of Jiangsu Province (BK20221406), the Innovation Program of Shanghai Municipal Education Commission (2021-01-07-00-02-E00106), and the Science and Technology Commission of Shanghai Municipality (22230780200 and 20DZ2250400), and Jiangsu Key Research and Development Project for Social Development Program (BE2022772). Besides, thanks for the support of the Analysis & Testing Center of Yancheng Institute of Technology.

## Appendix A. Supporting information

Supplementary data associated with this article can be found in the online version at doi:10.1016/j.apcatb.2024.123925.

## References

- [1] J. Seo, H. Nishiyama, T. Yamada, K. Domen, Visible-light-responsive photoanodes for highly active, stable water oxidation, *Angew. Chem. Int. Ed.* 57 (2018) 8396–8415.
- [2] K. Sivula, R. van de Krol, Semiconducting materials for photoelectrochemical energy conversion, *Nat. Rev. Mater.* 1 (2016) 15010.
- [3] S. Wang, G. Liu, L. Wang, Crystal facet engineering of photoelectrodes for photoelectrochemical water splitting, *Chem. Rev.* 119 (2019) 5192–5247.
- [4] B. Liu, S. Wang, G. Zhang, Z. Gong, B. Wu, T. Wang, J. Gong, Tandem cells for unbiased photoelectrochemical water splitting, *Chem. Soc. Rev.* 52 (2023) 4644–4671.
- [5] X. Li, S. Liu, K. Fan, Z. Liu, B. Song, J. Yu, MOF-based transparent passivation layer modified ZnO nanorod arrays for enhanced photo-electrochemical water splitting, *Adv. Energy Mater.* 8 (2018) 1800101.
- [6] P. Piangjai, Y. Jung-Ho, C. Hongjun, L. Miaoqiang, B. Teera, W. Lianzhou, Stable hematite nanosheet photoanodes for enhanced photoelectrochemical water splitting, *Adv. Mater.* 28 (2016) 6405–6410.
- [7] B. Zhang, L. Wang, Y. Zhang, Y. Ding, Y. Bi, Ultrathin FeOOH nanolayers with abundant oxygen vacancies on BiVO<sub>4</sub> photoanodes for efficient water oxidation, *Angew. Chem. Int. Ed.* 57 (2018) 2248–2252.
- [8] B. Zhang, X. Huang, Y. Zhang, G. Lu, L. Chou, Y. Bi, Unveiling the activity and stability origin of BiVO<sub>4</sub> photoanodes with FeNi oxyhydroxides for oxygen evolution, *Angew. Chem. Int. Ed.* 59 (2020) 18990–18995.
- [9] J.H. Kim, J.S. Lee, Elaborately modified BiVO<sub>4</sub> photoanodes for solar water splitting, *Adv. Mater.* 31 (2019) 1806938.
- [10] C.A. Bignozzi, S. Caramori, V. Cristina, R. Argazzi, L. Meda, A. Tacca, Nanostructured photoelectrodes based on WO<sub>3</sub>: applications to photooxidation of aqueous electrolytes, *Chem. Soc. Rev.* 42 (2013) 2228–2246.
- [11] M.B. Costa, M.A. de Araújo, M.Vd.L. Tinoco, J.Fd Brito, L.H. Mascaro, Current trending and beyond for solar-driven water splitting reaction on WO<sub>3</sub> photoanodes, *J. Energy Chem.* 73 (2022) 88–113.
- [12] G. Zheng, J. Wang, H. Liu, V. Murugadoss, G. Zu, H. Che, C. Lai, H. Li, T. Ding, Q. Gao, Z. Guo, Tungsten oxide nanostructures and nanocomposites for photoelectrochemical water splitting, *Nanoscale* 11 (2019) 18968–18994.
- [13] S.S. Kalanur, Y.J. Hwang, S.Y. Chae, O.S. Joo, Facile growth of aligned WO<sub>3</sub> nanorods on FTO substrate for enhanced photoanodic water oxidation activity, *J. Mater. Chem. A* 1 (2013) 3479–3488.
- [14] S. Ye, W. Shi, Y. Liu, D. Li, H. Yin, H. Chi, Y. Luo, N. Ta, F. Fan, X. Wang, C. Li, Unassisted photoelectrochemical cell with multimediator modulation for solar water splitting exceeding 4 % solar-to-hydrogen efficiency, *J. Am. Chem. Soc.* 143 (2021) 12499–12508.
- [15] L. Peter, Kinetics and Mechanisms of Light-driven Reactions at Semiconductor Electrodes: Principles and Techniques, Royal Society of Chemistry, Great Britain, 2013.
- [16] M. Ma, K. Zhang, P. Li, M.S. Jung, M.J. Jeong, J.H. Park, Dual oxygen and tungsten vacancies on a WO<sub>3</sub> photoanode for enhanced water oxidation, *Angew. Chem. Int. Ed.* 55 (2016) 11819–11823.
- [17] L. Yan, G. Dong, X. Huang, Y. Zhang, Y. Bi, Unraveling oxygen vacancy changes of WO<sub>3</sub> photoanodes for promoting oxygen evolution reaction, *Appl. Catal. B* 345 (2024) 123682.
- [18] S. Wang, H. Chen, G. Gao, T. Butburee, M. Lyu, S. Thaweesak, J.-H. Yun, A. Du, G. Liu, L. Wang, Synergistic crystal facet engineering and structural control of WO<sub>3</sub> films exhibiting unprecedented photoelectrochemical performance, *Nano Energy* 24 (2016) 94–102.
- [19] P.M. Rao, L. Cai, C. Liu, I.S. Cho, C.H. Lee, J.M. Weisse, P. Yang, X. Zheng, Simultaneously efficient light absorption and charge separation in WO<sub>3</sub>/BiVO<sub>4</sub> core/shell nanowire photoanode for photoelectrochemical water oxidation, *Nano Lett.* 14 (2014) 1099–1105.
- [20] L. Li, S. Xiao, R. Li, Y. Cao, Y. Chen, Z. Li, G. Li, H. Li, Nanotube array-like WO<sub>3</sub> photoanode with dual-layer oxygen-evolution cocatalysts for photoelectrocatalytic overall water splitting, *ACS Appl. Energy Mater.* 1 (2018) 6871–6880.
- [21] X. Feng, Y. Chen, Z. Qin, M. Wang, L. Guo, Facile fabrication of sandwich structured WO<sub>3</sub> nanoplate arrays for efficient photoelectrochemical water splitting, *ACS Appl. Mater. Interfaces* 8 (2016) 18089–18096.
- [22] J. Zhang, H. Ma, Z. Liu, Highly efficient photocatalyst based on all oxides WO<sub>3</sub>/Cu<sub>2</sub>O heterojunction for photoelectrochemical water splitting, *Appl. Catal. B* 201 (2017) 84–91.
- [23] J. Huang, Y. Zhang, Y. Ding, Rationally designed/constructed CoO<sub>x</sub>/WO<sub>3</sub> anode for efficient photoelectrochemical water oxidation, *ACS Catal.* 7 (2017) 1841–1845.
- [24] D. Jeon, N. Kim, S. Bae, Y. Han, J. Ryu, WO<sub>3</sub>/conducting polymer heterojunction photoanodes for efficient and stable photoelectrochemical water splitting, *ACS Appl. Mater. Interfaces* 10 (2018) 8036–8044.
- [25] J. Zhang, Z. Liu, Z. Liu, Novel WO<sub>3</sub>/Sb<sub>2</sub>S<sub>3</sub> heterojunction photocatalyst based on WO<sub>3</sub> of different morphologies for enhanced efficiency in photoelectrochemical water splitting, *ACS Appl. Mater. Interfaces* 8 (2016) 9684–9691.
- [26] M.G. Lee, D.H. Kim, W. Sohn, C.W. Moon, H. Park, S. Lee, H.W. Jang, Conformally coated BiVO<sub>4</sub> nanodots on porosity-controlled WO<sub>3</sub> nanorods as highly efficient type II heterojunction photoanodes for water oxidation, *Nano Energy* 28 (2016) 250–260.
- [27] Y. Zhou, L. Zhang, L. Lin, B.R. Wygant, Y. Liu, Y. Zhu, Y. Zheng, C.B. Mullins, Y. Zhao, X. Zhang, G. Yu, Highly efficient photoelectrochemical water splitting from hierarchical WO<sub>3</sub>/BiVO<sub>4</sub> nanoporous sphere arrays, *Nano Lett.* 17 (2017) 8012–8017.
- [28] Y. Dou, J. Zhou, A. Zhou, J.-R. Li, Z. Nie, Visible-light responsive MOF encapsulation of noble-metal-sensitized semiconductors for high-performance photoelectrochemical water splitting, *J. Mater. Chem. A* 5 (2017) 19491–19498.
- [29] J.W. Yoon, D.H. Kim, J.-H. Kim, H.W. Jang, J.-H. Lee, NH<sub>2</sub>-MIL-125(Ti)/TiO<sub>2</sub> nanorod heterojunction photoanodes for efficient photoelectrochemical water splitting, *Appl. Catal. B* 244 (2019) 511–518.
- [30] M. Ali, E. Pervaiz, T. Noor, O. Rabí, R. Zahra, M. Yang, Recent advancements in MOF-based catalysts for applications in electrochemical and photoelectrochemical water splitting: a review, *Int. J. Energy Res.* 45 (2021) 1190–1226.
- [31] C.F. Li, J.W. Zhao, L.J. Xie, J.Q. Wu, Q. Ren, Y. Wang, G.R. Li, Surface-adsorbed carboxylate ligands on layered double hydroxides/metal-organic frameworks promote the electrocatalytic oxygen evolution reaction, *Angew. Chem. Int. Ed.* 60 (2021) 18129–18137.
- [32] M. Jia, W. Xiong, Z. Yang, J. Cao, Y. Zhang, Y. Xiang, H. Xu, P. Song, Z. Xu, Metal-organic frameworks and their derivatives-modified photoelectrodes for photoelectrochemical applications, *Coord. Chem. Rev.* 434 (2021) 213780.
- [33] G. Dong, L. Yan, Y. Bi, Advanced oxygen evolution reaction catalysts for solar-driven photoelectrochemical water splitting, *J. Mater. Chem. A* 11 (2023) 3888–3903.
- [34] S. Li, Y. Gao, N. Li, L. Ge, X. Bu, P. Feng, Transition metal-based bimetallic MOFs and MOF-derived catalysts for electrochemical oxygen evolution reaction, *Energy Environ. Sci.* 14 (2021) 1897–1927.
- [35] L. Li, X. Zhao, D. Pan, G. Li, Nanotube array-like WO<sub>3</sub>/W photoanode fabricated by electrochemical anodization for photoelectrocatalytic overall water splitting, *Chin. J. Catal.* 38 (2017) 2132–2140.
- [36] T. Hisatomi, J. Kubota, K. Domen, Recent advances in semiconductors for photocatalytic and photoelectrochemical water splitting, *Chem. Soc. Rev.* 43 (2014) 7520–7535.
- [37] G. Kresse, J. Furthmüller, Efficient iterative schemes for ab initio total-energy calculations using a plane-wave basis set, *Phys. Rev. B* 54 (1996) 11169–11186.
- [38] F. Zhou, M. Cococcioni, C.A. Marianetti, D. Morgan, G. Ceder, First-principles prediction of redox potentials in transition-metal compounds with LDA+U, *Phys. Rev. B* 70 (2004) 235121.
- [39] A. Jain, G. Hautier, S.P. Ong, C.J. Moore, C.C. Fischer, K.A. Persson, G. Ceder, Formation enthalpies by mixing GGA and GGA + U calculations, *Phys. Rev. B* 84 (2011) 045115.
- [40] J. Rossmeisl, A. Logadottir, J.K. Nørskov, Electrolysis of water on (oxidized) metal surfaces, *Chem. Phys.* 319 (2005) 178–184.
- [41] J. Du, X. Zhong, H. He, J. Huang, M. Yang, G. Ke, J. Wang, Y. Zhou, F. Dong, Q. Ren, L. Bian, Enhanced photoelectrochemical water oxidation performance on BiVO<sub>4</sub> by coupling of CoMoO<sub>4</sub> as a hole-transfer and conversion cocatalyst, *ACS Appl. Mater. Interfaces* 10 (2018) 42207–42216.
- [42] Y. Liu, J. Li, W. Li, Y. Yang, Y. Li, Q. Chen, Enhancement of the photoelectrochemical performance of WO<sub>3</sub> vertical arrays film for solar water splitting by gadolinium doping, *J. Phys. Chem. C* 119 (2015) 14834–14842.
- [43] S. Zhou, K. Chen, J. Huang, L. Wang, M. Zhang, B. Bai, H. Liu, Q. Wang, Preparation of heterometallic CoNi-MOFs-modified BiVO<sub>4</sub>: a steady photoanode for improved performance in photoelectrochemical water splitting, *Appl. Catal. B* 266 (2020) 118513.
- [44] J. Yang, P. Xiong, C. Zheng, H. Qiu, M. Wei, Metal-organic frameworks: a new promising class of materials for a high performance supercapacitor electrode, *J. Mater. Chem. A* 2 (2014) 16640–16644.
- [45] Y. Yan, P. Gu, S. Zheng, M. Zheng, H. Pang, H. Xue, Facile synthesis of an accordion-like Ni-MOF superstructure for high-performance flexible supercapacitors, *J. Mater. Chem. A* 4 (2016) 19078–19085.
- [46] J.G. Vitillo, L. Regli, S. Chavan, G. Ricchiardi, G. Spoto, P.D. Dietzel, S. Bordiga, A. Zecchina, Role of exposed metal sites in hydrogen storage in MOFs, *J. Am. Chem. Soc.* 130 (2008) 8386–8396.
- [47] P. Wen, P. Gong, J. Sun, J. Wang, S. Yang, Design and synthesis of Ni-MOF/CNT composites and rGO/carbon nitride composites for an asymmetric supercapacitor with high energy and power density, *J. Mater. Chem. A* 3 (2015) 13874–13883.

- [48] Q. Ma, R. Song, F. Ren, H. Wang, W. Gao, Z. Li, C. Li, Photoelectrocatalytic degradation of refractory pollutants over  $\text{WO}_3/\text{W}$  network photoelectrode with heterophase junction for enhancing mass transportation and charge separation, *Appl. Catal. B* 309 (2022) 121292.
- [49] F. Shahbazi Farahani, M.S. Rahamanifar, A. Noori, M.F. El-Kady, N. Hassani, M. Neek-Amal, R.B. Kaner, M.F. Mousavi, Trilayer metal-organic frameworks as multifunctional electrocatalysts for energy conversion and storage applications, *J. Am. Chem. Soc.* 144 (2022) 3411–3428.
- [50] A. Krylov, A. Vtyurin, P. Petkov, I. Senkovska, M. Maliuta, V. Bon, T. Heine, S. Kaskel, E. Slyusareva, Raman spectroscopy studies of the terahertz vibrational modes of a DUT-8 (Ni) metal-organic framework, *Phys. Chem. Chem. Phys.* 19 (2017) 32099–32104.
- [51] Y. Jin, G. Xu, X. Li, J. Ma, L. Yang, Y. Li, H. Zhang, Z. Zhang, D. Yao, D. Li, Fast cathodic reduction electrodeposition of a binder-free cobalt-doped Ni-MOF film for directly sensing of levofloxacin, *J. Alloy. Compd.* 851 (2021) 156823.
- [52] Y. Du, M. Zhang, Z. Wang, Y. Liu, Y. Liu, Y. Geng, L. Wang, A self-templating method for metal-organic frameworks to construct multi-shelled bimetallic phosphide hollow microspheres as highly efficient electrocatalysts for hydrogen evolution reaction, *J. Mater. Chem. A* 7 (2019) 8602–8608.
- [53] D. Pan, S. Xiao, X. Chen, R. Li, Y. Cao, D. Zhang, S. Pu, Z. Li, G. Li, H. Li, Efficient photocatalytic fuel cell via simultaneous visible-photoelectrocatalytic degradation and electricity generation on a porous coral-like  $\text{WO}_3/\text{W}$  photoelectrode, *Environ. Sci. Technol.* 53 (2019) 3697–3706.
- [54] L. Xia, J. Bai, J. Li, Q. Zeng, X. Li, B. Zhou, A highly efficient  $\text{BiVO}_4/\text{WO}_3/\text{W}$  heterojunction photoanode for visible-light responsive dual photoelectrode photocatalytic fuel cell, *Appl. Catal. B* 183 (2016) 224–230.
- [55] J.M. Macak, H. Tsuchiya, A. Ghicov, K. Yasuda, R. Hahn, S. Bauer, P. Schmuki,  $\text{TiO}_2$  nanotubes: self-organized electrochemical formation, properties and applications, *Curr. Opin. Solid State Mater. Sci.* 11 (2007) 3–18.
- [56] P.D. Dietzel, B. Panella, M. Hirscher, R. Blom, H. Fjellvag, Hydrogen adsorption in a nickel based coordination polymer with open metal sites in the cylindrical cavities of the desolvated framework, *Chem. Commun.* (2006) 959–961.
- [57] S. Zhao, Y. Wang, J. Dong, C.-T. He, H. Yin, P. An, K. Zhao, X. Zhang, C. Gao, L. Zhang, J. Lv, J. Wang, J. Zhang, A.M. Khattak, N.A. Khan, Z. Wei, J. Zhang, S. Liu, H. Zhao, Z. Tang, Ultrathin metal-organic framework nanosheets for electrocatalytic oxygen evolution, *Nat. Energy* 1 (2016) 16184.
- [58] J. Duan, S. Chen, C. Zhao, Ultrathin metal-organic framework array for efficient electrocatalytic water splitting, *Nat. Commun.* 8 (2017) 15341.
- [59] F. Kurnia, Y.H. Ng, Y. Tang, R. Amal, N. Valanoor, J.N. Hart,  $\text{ZnS}$  thin films for visible-light active photoelectrodes: effect of film morphology and crystal structure, *Cryst. Growth Des.* 16 (2016) 2461–2465.
- [60] F. Wu, J. Xie, Y. You, Z. Zhao, L. Wang, X. Chen, P. Yang, Y. Huang, Cobalt metal-organic framework ultrathin cocatalyst overlayer for improved photoelectrochemical activity of Ti-doped hematite, *ACS Appl. Energy Mater.* 3 (2020) 4867–4876.
- [61] K. Wang, Y. Liu, K. Kawashima, X. Yang, X. Yin, F. Zhan, M. Liu, X. Qiu, W. Li, C. B. Mullins, J. Li, Modulating charge transfer efficiency of hematite photoanode with hybrid dual-metal-organic frameworks for boosting photoelectrochemical water oxidation, *Adv. Sci.* 7 (2020) 2002563.
- [62] H. Yang, J. Bright, S. Kasani, P. Zheng, T. Moshu, B. Chen, L. Huang, N. Wu, Metal-organic framework coated titanium dioxide nanorod array p-n heterojunction photoanode for solar water-splitting, *Nano Res.* 12 (2019) 643–650.
- [63] W. Li, K. Wang, X. Yang, F. Zhan, Y. Wang, M. Liu, X. Qiu, J. Li, J. Zhan, Q. Li, Y. Liu, Surfactant-assisted controlled synthesis of a metal-organic framework on  $\text{Fe}_2\text{O}_3$  nanorod for boosted photoelectrochemical water oxidation, *Chem. Eng. J.* 379 (2020) 122256.
- [64] Y. He, T. Hamann, D. Wang, Thin film photoelectrodes for solar water splitting, *Chem. Soc. Rev.* 48 (2019) 2182–2215.
- [65] X. Sheng, T. Xu, X. Feng, Rational design of photoelectrodes with rapid charge transport for photoelectrochemical applications, *Adv. Mater.* 31 (2019) 1805132.
- [66] D.-J. Li, Q.-H. Li, Z.-G. Gu, J. Zhang, A surface-mounted MOF thin film with oriented nanosheet arrays for enhancing the oxygen evolution reaction, *J. Mater. Chem. A* 7 (2019) 18519–18528.
- [67] L. Huang, G. Gao, H. Zhang, J. Chen, Y. Fang, S. Dong, Self-dissociation-assembly of ultrathin metal-organic framework nanosheet arrays for efficient oxygen evolution, *Nano Energy* 68 (2020) 104296.
- [68] W. Zhou, D.-D. Huang, Y.-P. Wu, J. Zhao, T. Wu, J. Zhang, D.-S. Li, C. Sun, P. Feng, X. Bu, Stable hierarchical bimetal-organic nanostructures as highperformance electrocatalysts for the oxygen evolution reaction, *Angew. Chem. Int. Ed.* 58 (2019) 4227–4231.
- [69] B. Wang, J. Shang, C. Guo, J. Zhang, F. Zhu, A. Han, J. Liu, A general method to ultrathin bimetal-MOF nanosheets arrays via *in situ* transformation of layered double hydroxides arrays, *Small* 15 (2019) 1804761.
- [70] C.-W. Kung, J.E. Mondloch, T.C. Wang, W. Bury, W. Hoffeditz, B.M. Klahr, R. C. Klet, M.J. Pellin, O.K. Farha, J.T. Hupp, Metal-organic framework thin films as platforms for atomic layer deposition of cobalt ions to enable electrocatalytic water oxidation, *ACS Appl. Mater. Interfaces* 7 (2015) 28223–28230.
- [71] S. Ye, C. Ding, R. Chen, F. Fan, P. Fu, H. Yin, X. Wang, Z. Wang, P. Du, C. Li, Mimicking the key functions of photosystem II in artificial photosynthesis for photoelectrocatalytic water splitting, *J. Am. Chem. Soc.* 140 (2018) 3250–3256.
- [72] G.L. Chiarello, M. Bernareggi, M. Pedroni, M. Magni, S.M. Pietralunga, A. Tagliaferri, E. Vassallo, E. Sellì, Enhanced photopromoted electron transfer over a bilayer  $\text{WO}_3$  n-n heterojunction prepared by RF diode sputtering, *J. Mater. Chem. A* 5 (2017) 12977–12989.
- [73] B. Klahr, S. Gimenez, F. Fabregat-Santiago, J. Bisquert, T.W. Hamann, Photoelectrochemical and impedance spectroscopic investigation of water oxidation with "Co-Pi"-coated hematite electrodes, *J. Am. Chem. Soc.* 134 (2012) 16693–16700.
- [74] M. Gong, Y. Li, H. Wang, Y. Liang, J.Z. Wu, J. Zhou, J. Wang, T. Regier, F. Wei, H. Dai, An advanced Ni-Fe layered double hydroxide electrocatalyst for water oxidation, *J. Am. Chem. Soc.* 135 (2013) 8452–8455.
- [75] J. Wang, J. Liu, B. Zhang, H. Wan, Z. Li, X. Ji, K. Xu, C. Chen, D. Zha, L. Miao, J. Jiang, Synergistic effect of two actions sites on cobalt oxides towards electrochemical water-oxidation, *Nano Energy* 42 (2017) 98–105.
- [76] Y. Jin, S. Huang, X. Yue, C. Shu, P.K. Shen, Highly stable and efficient non-precious metal electrocatalysts of Mo-doped  $\text{NiOOH}$  nanosheets for oxygen evolution reaction, *Int. J. Hydrogen Energy* 43 (2018) 12140–12145.
- [77] Y. Kuang, Q. Jia, H. Nishiyama, T. Yamada, A. Kudo, K. Domen, A front-illuminated nanostructured transparent  $\text{BiVO}_4$  photoanode for >2 % efficient water splitting, *Adv. Energy Mater.* 6 (2016) 1501645.
- [78] T.W. Kim, K.S. Choi, Nanoporous  $\text{BiVO}_4$  photoanodes with dual-layer oxygen evolution catalysts for solar water splitting, *Science* 343 (2014) 990–994.
- [79] J. Yang, L. Li, C. Xiao, Y. Xie, Dual-plasmon resonance coupling promoting directional photosynthesis of nitrate from air, *Angew. Chem. Int. Ed.* 62 (2023) e202311911.
- [80] Y. Zhang, Y. Li, D. Ni, Z. Chen, X. Wang, Y. Bu, J.-P. Ao, Improvement of  $\text{BiVO}_4$  photoanode performance during water photo-oxidation using Rh-doped  $\text{SrTiO}_3$  perovskite as a Co-catalyst, *Adv. Funct. Mater.* 29 (2019) 1902101.
- [81] B. Zhang, S. Yu, Y. Dai, X. Huang, L. Chou, G. Lu, G. Dong, Y. Bi, Nitrogen-incorporation activates  $\text{NiFeO}_x$  catalysts for efficiently boosting oxygen evolution activity and stability of  $\text{BiVO}_4$  photoanodes, *Nat. Commun.* 12 (2021) 6969.
- [82] A. Birsan, V. Kuncser, First principle investigations of the structural, electronic and magnetic properties of predicted new zirconium based full-Heusler compounds,  $\text{Zr}_2\text{MnZ}$  ( $Z=\text{Al}, \text{Ga}$  and  $\text{In}$ ), *J. Magn. Magn. Mater.* 406 (2016) 282–288.
- [83] F.R. McFeeley, S.P. Kowalczyk, L. Ley, R.G. Cavell, R.A. Pollak, D.A. Shirley, X-ray photoemission studies of diamond, graphite, and glassy carbon valence bands, *Phys. Rev. B* 9 (1974) 5268–5278.
- [84] Y. Zhou, Z. Zhou, R. Shen, R. Ma, Q. Liu, G. Cao, J. Wang, Correlating electrocatalytic oxygen reduction activity with d-band centers of metallic nanoparticles, *Energy Storage Mater.* 13 (2018) 189–198.
- [85] A. Vojdovic, J.K. Norskov, Optimizing perovskites for the water-splitting reaction, *Science* 334 (2011) 1355–1356.
- [86] J. Suntivich, K.J. May, H.A. Gasteiger, J.B. Goodenough, Y. Shao-Horn, A perovskite oxide optimized for oxygen evolution catalysis from molecular orbital principles, *Science* 334 (2011) 1383–1385.
- [87] J.Y. Chen, L. Dang, H. Liang, W. Bi, J.B. Gerken, S. Jin, E.E. Alp, S.S. Stahl, Operando analysis of NiFe and Fe oxyhydroxide electrocatalysts for water oxidation: detection of  $\text{Fe}^{4+}$  by Mossbauer spectroscopy, *J. Am. Chem. Soc.* 137 (2015) 15090–15093.
- [88] X. Zheng, X. Wu, L. Zhang, J. Kang, M. Zhou, Y. Zhong, J. Zhang, L. Wang, High spin  $\text{Fe}^{3+}$ -related bonding strength and electron transfer for sensitive and stable SERS detection, *Chem. Sci.* 13 (2022) 12560–12566.